The grain-scale signature of isotopic diffusion in ice

Felix S. L. Ng[1]

[1]Department of Geography, University of Sheffield, Sheffield, UK

Correspondence: Felix Ng (f.ng@sheffield.ac.uk)

Abstract. Diffusion limits the survival of climate signals on ice-core isotopic records. Diffusive smoothing acts not only on annual signals near the surface, but also on long time-scale signals at depth as they shorten to decimetres or centimetres. Short-circuiting of the slow diffusion in crystal grains by fast diffusion along liquid veins can explain the "excess diffusion" found on some records. But direct experimental evidence is lacking whether this mechanism operates as theorised; current theories of the short-circuiting also under-explore the role of diffusion along grain boundaries. The nonuniform patterns of isotope concentration across crystal grains induced by the short-circuiting offer a testable prediction of these theories. Here, we extend the modelling for grain boundaries (as well as veins) and calculate these patterns for different grain-boundary diffusivities and thicknesses, temperatures, and vein-water flow velocities. Two isotopic patterns are shown to prevail in ice of millimetre grain size: (i) an axisymmetric "pole" pattern with excursions in δ centred on triple junctions, in the case of thin, low-diffusivity grain boundaries; (ii) a "spoke" pattern with excursions around triple junctions showing the impression of grain boundaries, when these are thick and highly diffusive. The excursions have widths ~ 0.1–0.5 of the grain radius and variations in $\delta \sim 10^{-2}$ to 10^{-1} of the bulk isotopic signal, which set the minimum required measurement capability for laser-ablation mapping to detect them. We examine how the predicted patterns vary with depth through a bulk-signal wavelength to suggest an experimental procedure of testing ice-core samples for these signatures of isotopic short-circuiting. Because our model accounts for veins and grain boundaries, its predicted enhancement factor (quantifying the level of excess diffusion) characterises the bulk isotopic diffusivity more comprehensively than past studies.

1 Introduction

The water stable isotope records (δ^{18}O, δD) in polar ice cores contain diverse palaeoclimatic signals. Owing to isotopic diffusion in firn and ice, signals at the decimetre and centimetre or shorter scales experience pronounced smoothing as they descend the ice column. This postdepositional process limits the integrity and resolution of climatic information at different depths. The smoothing rate needs to be known for recovering the original (e.g. annual) δ variations at the surface by "back

35 diffusing" an isotopic record (Johnsen, 1977), reconstructing surface temperatures in the past from spectrally-derived diffusion lengths (Gkinis et al., 2014), and predicting how deep climatic signals of different time scales survive into an ice core (e.g. Grisart et al., 2022). The last aspect, which matters particularly for long records, is of major interest to the ongoing ice-coring campaigns at Little Dome C, East Antarctica, which aim to retrieve ice reaching back ~ 1–1.5 Ma.

"Excess diffusion" in the ice below the firn is a key concern in this subject. Analysis of the GRIP (Greenland Ice Core

40 Project) ice core by Johnsen et al. (1997, 2000) showed that the annual δ^{18}O signals in the Holocene section of this core decay ~ 10–30 times faster than expected from the self-diffusion rate measured in single ice crystals (Ramseier, 1967), implying a large enhancement of the bulk-ice isotopic diffusivity above the monocrystal diffusivity. Theories put forward to explain this excess diffusion invoke short-circuiting – the idea that, in polycrystalline ice, fast diffusion in the network of liquid veins (located at triple junctions) and along grain boundaries bypasses the slow diffusion within ice grains to cause the enhancement.

45 After Nye (1998) made pioneering calculations to show that the presence of veins causes excess diffusion by short-circuiting, Johnsen et al. (2000) adapted the firn isotope diffusion model of Whillans and Grootes (1985) to gauge the separate contributions of grain boundaries and veins to the mechanism. Later, Rempel and Wettlaufer (2003) refined Nye's model to account for the finite isotopic diffusivity of the vein water; they calculated the diffusivity enhancement in ice at $\approx$ –32 °C as a function of signal wavelength, grain size, and vein radius. In a recent study, Ng (2023) extended the Nye–Rempel–Wettlaufer

50 framework to show that water flow in the veins amplifies excess diffusion, and that vein-water flow velocities of ~10^1–10^2 m yr^{-1} yield a ten to hundred fold enhancement, able to explain the GRIP findings and sections of ice with anomalously high diffusion lengths found in the EPICA (European Project for Ice Coring in Antarctica) Dome C ice core by Pol et al. (2010) and found in the WAIS (West Antarctic Ice Sheet) Divide ice core by Jones et al. (2018) – which these authors interpreted as signs of excess diffusion. As pointed out by Ng (2023), the modulation of isotopic diffusion by vein-water flow means that the

55 decay of climate signals at each ice-core site depends on the hydrology and connectivity of veins down the ice column, as well as the ice temperature, grain and vein sizes, and recrystallisation processes affecting these geometries.

Here, we take the modelling of excess diffusion in a new direction to enable a critical research gap to be addressed. Besides those records displaying signs of excess diffusion (accelerated signal decay or anomalous diffusion lengths) and motivating the theories in the first place, no direct observations have been made to show that isotopic short-circuiting actually

60 operates. Independent evidence is needed to verify the mechanism at the grain scale, for ice-core samples deemed affected by excess diffusion, and for polycrystalline ice generally. One way of testing the theories is to compare their predicted signal

smoothing rate against the rate measured in ice doped with isotopic signals, but the slowness of diffusion makes such experiments prohibitively long at low temperature. Another laboratory-based approach, proposed herein, is to analyse ice affected by excess diffusion to look for the distinct grain-scale isotopic variations which the theories predict to result from
65   short-circuiting. For instance, the theories of Nye (1998), Rempel and Wettlaufer (2003) and Ng (2023) – capturing isotopic exchange between veins and ice and ignoring grain boundaries – imply axisymmetric patterns of δ around veins, which may be used for this purpose. Knowledge of these patterns is prerequisite to testing for short-circuiting this way. Predicting their variety forms the main goal of this paper, although we leave the laboratory work to future studies.

To simulate realistic isotopic patterns, we go beyond the past theories by formulating a continuum model that includes
70   grain boundaries, coupling diffusion across all three components: ice, veins, and grain boundaries. The model geometry, which remains simplified, allows us to explore the combined effect of veins and grain boundaries on the bulk-ice isotopic diffusivity. An outstanding question in this regard is whether diffusion along grain boundaries matters in ice with glaciological grain sizes (~ mm). Their effect on the bulk diffusivity is assumed to be significant in ultra fine-grained ice with ~ 10–30 nm sized crystals (Lu et al., 2009), where grain-boundary surfaces have a high volumetric density (Jones et al. 2017). In contrast, for glacier ice,
75   a much weaker effect may be suspected based on the calculations of Johnsen et al. (2000), who estimated that the grain boundaries in the GRIP Holocene ice (mean grain diameter ≈ 3 mm) need to be unrealistically thick (50 nm) to explain the observed excess diffusion, even if they are liquid films with the high isotopic diffusivity of water. Studying this question with a fully-coupled model has not been done before and forms our second goal. We compute the enhancement factor f for ice of millimetre grain size at –32 ℃ and –52 ℃ (which approximate the upper column temperatures at the GRIP and EPICA core
80   sites, respectively) for different grain-boundary properties and vein-water flow velocities.

Including grain boundaries in the modelling brings challenges. Most obviously, the grain-boundary thickness c and grain-boundary diffusivity D_b need to be specified; but as we will elaborate in Sect. 2, these parameters are not well constrained. In our calculations, we cover potential scenarios by experimenting with different assumptions for c and D_b in a sensitivity analysis. Another issue is that the model geometry does not permit analytical solution, unlike in the theories of Nye (1998),
85   Rempel and Wettlaufer (2003), and Ng (2023). We tackle this by developing a bespoke numerical solution method.

The paper is organised as follows. Sect. 2 details model formulation and our solution method. Sect. 3 presents computed isotopic patterns and enhancement factors for a range of parameters, including the end-member cases of thick, diffusive and thin, non-diffusive grain boundaries and intermediate scenarios. In Sect. 4, we discuss the prospects of detecting the isotopic signatures of excess diffusion in laboratory measurements on ice, focussing on techniques based on laser-ablation sampling.
90   Readers keen to see the predicted patterns are advised to turn to Figs. 4–11. Those seeking to compute the diffusivity enhancement factor for conditions not covered by us can find our numerical code in the repository linked to the paper.

2 Mathematical model

2.1 *Model geometry*

We use the set-up in Fig. 1a – adapted from Nye (1998), Rempel and Wettlaufer (2003) and Ng (2023), which represents ice
95 crystal grains surrounding a vein by a vertical annular cylinder, in $a \le r \le b$, where r is the radial coordinate, a is the vein radius (~ μm), and b approximates the mean grain radius (~ mm). The water vein is kept liquid by dissolved ionic impurities, which lower the melting point (Mulvaney et al., 1988; Nye, 1991; Mader, 1992b). We consider depth-varying isotopic signals in the bulk ice, with z denoting depth.

Grain boundaries leading from the vein are modelled as planes of thickness c ($\ll a$) at $\theta = 0$, L, and $2L$, where θ is the
100 azimuth and $L = 2\pi/3$. Introducing them makes the problem non-axisymmetric, but their periodicity means that it suffices to solve the model in $0 \le \theta \le L$.

In plan view, the cylinder approximates a unit cell centred upon triple junctions in ice whose structure is idealised as honeycomb-like (Fig. 1b). In this picture, the radius b reaches out roughly half-way along each grain boundary or to the middle of grains; for convenience, we refer to $r \approx b$ at either location as the "interior". Like the original theories, our extended model
105 geometry still idealises many aspects of the real system: (1) It ignores the detailed vein cross-section, which consists of three convex walls (Nye, 1989; Mader, 1992a; Ng, 2021), although their small length-scale will perturb only the local isotopic concentrations near $r = a$. (2) The veins and grain boundaries are assumed stationary, rather than migrating under recrystallisation processes. (3) Horizontal or near-horizontal veins and grain boundaries are disregarded; thus the model does not account for additional short-circuiting arising from these boundaries, which will distort the isotopic patterns near them and
110 influence the enhancement factor. We discuss the last two limitations in more detail in Sect. 4.
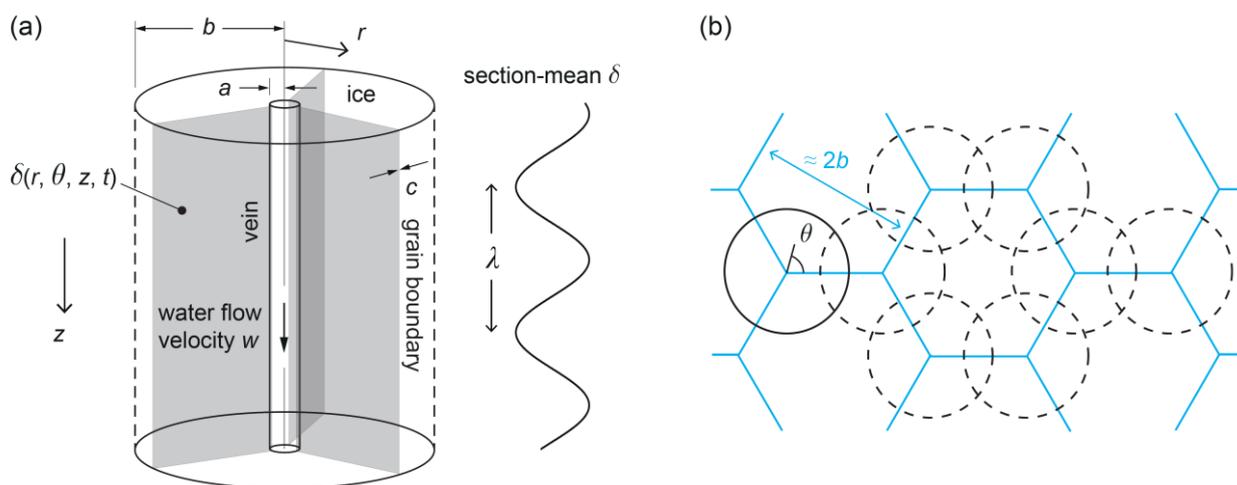
Figure 1. (a) Model geometry for calculating coupled isotopic diffusion in ice, vein, and grain boundaries near a triple junction. (b) Approximate view of what the cell in panel (a) represents in polycrystalline ice with hexagonal grains.

115 2.2 *Material properties*

Prior to modelling signal evolution, we consider the isotopic diffusivities in the three components (ice, vein-water, grain boundaries) and the grain-boundary thickness and, where relevant, explain values chosen for simulations. All diffusivities discussed here – referring to molecular diffusion – are applicable to the transport of oxygen and deuterium.

For the isotopic diffusivity in ice or "solid diffusivity" D_s, we use Ramseier's (1967) formula for self-diffusion in single

120 ice crystals:

$$D_s = 9.1 \times 10^{-4} \exp\left(-\frac{7.2 \times 10^3}{T}\right) \ \text{m}^2 \ \text{s}^{-1},$$ (1)

in which T denotes temperature. For the isotopic diffusivity in vein-water or "liquid diffusivity" D_v, we use the composite exponential formula:

$$D_v = \frac{1}{\dfrac{1}{1.085 \times 10^{-6} \exp\left(\dfrac{-1870}{T}\right)} + \dfrac{1}{2.942 \times 10^7 \exp\left(\dfrac{-9474}{T}\right)}} \ \text{m}^2 \ \text{s}^{-1}.$$ (2)

125 This formula was derived by Ng (2023) by fitting self-diffusivity data between –12.8 °C and –60.8 °C, which Xu et al. (2016) obtained by modelling crystal-growth rates measured in laboratory experiments. Eqn. (2) is consistent with the established formula of Gillen et al. (1972) for T down to –31 °C but covers a greater temperature range. Fig. 2 plots Eqns. (1) and (2). These formulas do not account for pressure dependence, which should cause only a minor correction under the glaciostatic overburden in ice sheets (a few % on D_v; Prielmeier et al., 1988), nor the influence of dissolved impurities, whose characterisation is presently very limited. Thus, D_s and D_v might vary from the formulas. However, the temperature

130 dependences shown in Fig. 2 should be robust, and departures from the formulas by a few times (e.g. see uncertainty for D_s indicated by Lu et al. (2009) in their Fig. 8) or even an order of magnitude are much smaller than the diffusivity contrast D_v/D_s ~ 10^6, which governs the qualitative interactions during vein short-circuiting.

What of the grain-boundary diffusivity D_b and thickness c? The physico-chemical influences on these parameters are

135 poorly understood across the range of ice-core temperatures (~ 0 to –55 °C); their values are uncertain and lack reliable formulas. Several empirical and theoretical constraints come to our rescue, as detailed below. But first we sketch more background on the grain-boundary properties of ice, as a step towards explaining our choices for these parameters.

Grain boundaries are disordered interfaces between crystals. Determining their properties experimentally is difficult because the microscopic scale concerned means that often a property can only be inferred from bulk measurements that mix

140 crystal and grain-boundary effects. In ice, the grain-boundary thickness must be at least several times crystal lattice spacing (O–O distance: 0.276 nm) but may be much higher in the presence of impurities. *Premelting* occurs at high temperature (Dash et al., 2006): grain boundaries thicken and start to exhibit quasi-liquid behaviour near the melting point T_m as this is approached
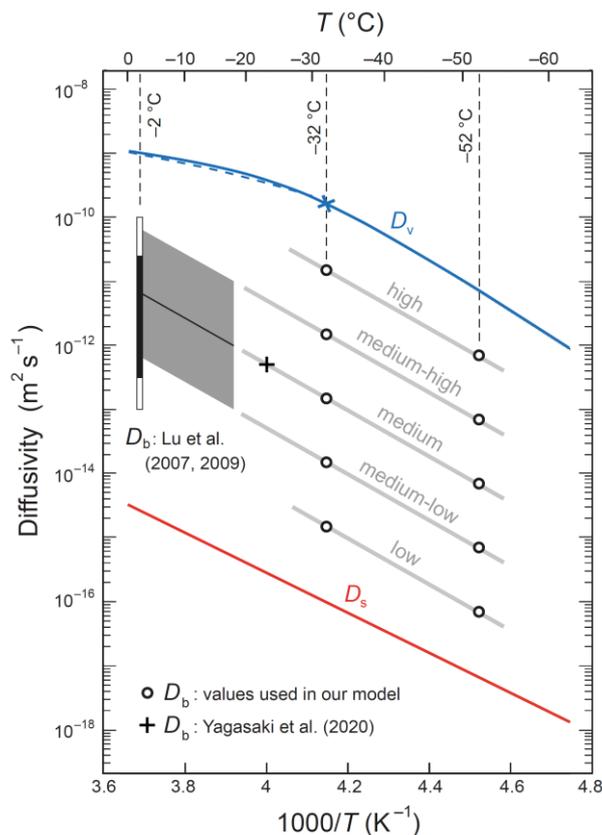
Figure 2. Arrhenius plot of the isotopic diffusivities D_s (ice), D_v (vein water) and D_b (grain boundaries). The curves for D_s and D_v come from

145 Eqs. (1) and (2). Blue dashed curve plots Gillen et al.'s (1972) relation for D_v. Blue cross locates the diffusivity used by Johnsen et al. (2000) (see text). On the left, the composite bar at –2 °C (black: likely range; white: maximal range) and the inclined grey band (central value with uncertainty) indicate the laboratory-based estimates for D_b of Lu et al. (2007) and Lu et al. (2009), respectively. Black cross plots D_b at 250 K from molecular dynamical simulation. Black circles show the values of D_b experimented in our modelling, also listed in Table 1. The grey lines through them, constructed from the trend of the grey band, convey our descriptive diffusivity scale (Sect. 3).

150

from below: at $T_m - T = 0$ to ~10 K. Grain-boundary premelting in ice has been studied by (i) theoretical modelling of the forces and thermodynamics controlling the premelted film thickness (Wettlaufer, 1999; Benatov and Wettlaufer, 2004), (ii) laboratory measurements of the film thickness under different conditions (Thomson et al., 2013), and (iii) classical molecular dynamical simulations (e.g. Moreira et al., 2018). Premelting in ice diminishes beyond a few °C below T_m and is expected to

155 be negligible below $\sim$ –10 °C. For instance, Lu et al. (2007, 2009) argued from experimental results for D_b (reported below) that premelting does not occur below –2 °C in pure ice, although it starts to occur at ≈ –8 °C in ice doped with HCl at 0.04% by mass (≈ 0.01 M bulk concentration). On the other hand, the notion of premelted grain boundaries features in Johnsen et al.'s (2000) and Rempel and Wettlaufer's (2003) theories of excess diffusion, even though their analyses considered much

colder ice. Johnsen et al. (2000), particularly, referred to the grain boundaries in ice at $T = -32$ °C as "supercooled water films"
160 and took the liquid diffusivity D_v (blue cross, Fig. 2) as the grain-boundary diffusivity D_b in calculations. As we will see, this
estimate for D_b is probably too high.

The question whether grain boundaries in ice are watery or more like disrupted solid lattice has bearing on where isotope
fractionation (during phase change) is envisaged to occur in the system. In our model, we assume fractionation where grain
boundaries meet the vein, not where they transition into crystal lattice. The reverse assumption seems less plausible because
165 our simulations explore temperatures far below the premelting regime. Note, however, that the question is unsettled given the
lack of experimental determination: fractionation may occur at both places in reality.

We turn to the parameter choices, treating grain-boundary thickness c first. Information comes from two studies.
Thomson et al. (2013) used optical scattering to measure c in ice at $T \approx -1.5$ °C with different dissolved impurity concentrations
(NaCl) and different grain-boundary orientations. The impurity concentration at grain boundaries was estimated from bulk
170 concentration as it cannot be measured directly. They found c from 1 to 8 nm, generally increasing with the impurity level
(this factor promotes interfacial molecular disorder) at different crystal misorientation angles. For $T < -1.5$ °C, no experimental
measurements have been made so far, but molecular-scale dynamical simulations give a handle on c. Yagasaki et al. (2020)
used the TIP4P/Ice model to study molecular transport at grain boundaries in impurity-free ice at 250 K (≈ -23 °C) and found
$c \sim 1$ nm under a variety of conditions. Given these studies, we choose three values of c for our modelling: 1 nm, 5 nm and 10
175 nm. The highest value accounts for the possibility of thick grain boundaries resulting from high impurity levels.

For the grain-boundary diffusivity D_b, we rely on the experimental results of Lu et al. (2007, 2009), which are the only
results available to date on ice. For T from -18 °C to -1 °C, these authors determined that D_b lies intermediate between D_s and
D_v (Fig. 2), several orders of magnitude from each of them and showing an Arrhenius dependence with an activation energy
of ≈ 69 kJ mol^{-1}. Their experiments measured the inter-diffusivity D_{eff} of H and D in nanocrystalline sandwiches of
180 H$_2$O/D$_2$O/H$_2$O ice by monitoring the reaction zones at the interfaces with thermal desorption spectroscopy, a technique that
ablates the ice with laser and analyses the vapour composition. They estimated D_b from D_{eff} by a model inversion based on the
Hart–Mortlock equation (D_{eff} as a linear combination of the component diffusivities, weighted by the component volume
fractions). In their 2007 study, conducted at -2 °C, their D_b estimate spans 3 orders of magnitude, although they suggested a
likely range of 1–2 orders (vertical bar, Fig. 2). Their 2009 study extended measurements down to -18 °C, yielding the black
185 line for D_b in Fig. 2, with an order of magnitude uncertainty on either side (grey band). To pose D_b values for modelling, we
extrapolate their estimated range for D_b to lower temperatures down the Arrhenius trend. This approach finds support in the
modelled value of D_b at 250 K from Yagasaki et al. (2020) (black cross, Fig. 2). But we widen the uncertainty range of Lu et
al. because (i) the Hart–Mortlock equation crudely approximates the bulk diffusivity[1], and the version of the equation used in

---

[1] That the Hart–Mortlock equation may only roughly approximate the bulk/effective diffusivity in some applications has been recognised
(e.g. Lundy, 1978). Moreover, for the coupled diffusion studied here, our results (Sect. 3.2) imply a bulk diffusivity varying with signal
wavelength, not what the Hart–Mortlock equation would predict.

190 Table 1: Isotopic diffusivities (in $m^2\ s^{-1}$) used in our modelling. At each temperature, we investigate five values of the grain-boundary diffusivity, D_b.

	$T = -32$ °C	$T = -52$ °C
D_v	1.65×10^{-10}	7.08×10^{-12}
D_b	1.5×10^{-11}	7×10^{-13}
	1.5×10^{-12}	7×10^{-14}
	1.5×10^{-13}	7×10^{-15}
	1.5×10^{-14}	7×10^{-16}
	1.5×10^{-15}	7×10^{-17}
D_s	9.83×10^{-17}	6.60×10^{-18}

195 their inversion ignores the presence of veins, and (ii) they showed that doping the ice with HCL increased D_{eff} by ~ 20 times above the pure-ice value, indicating that dissolved impurities can raise D_b substantially. Uncertainties in the inversion from assumptions about the grain-boundary width are discussed by Lu et al. (2007) also. Consequently, we choose two sets of five values for D_b (circles in Fig. 2): one set for –32 °C and the other for –52 °C. At each temperature, the middle three values of D_b represent extensions of Lu et al.'s findings; the lowest value yields results near the no-grain-boundary limit; the highest

200 value mimics scenarios of high impurity concentration at grain boundaries (ice-core samples can be very variable in these). Listed in Table 1, the diffusivities span generous ranges for our sensitivity experiments. We explore select values of D_b and c, given the impracticality of covering a large number of parameter combinations when computing isotopic patterns and enhancement factors.

That D_b is bracketed by D_s and D_v corroborate insights from classical molecular dynamical simulations. Moreira et al.
205 (2018) found that a few degrees below T_m, the simulated molecular transport along premelted grain boundaries resembles diffusion in glassy systems and is sub-diffusive in character (with mean-square displacement ~ t^γ, where $\gamma < 1$), reflecting lateral confinement of the grain boundaries by adjacent crystal lattice. The grain boundaries at 250 K simulated by Yagasaki et al. (2020) structurally resemble low-density liquid water. Besides estimating a corresponding value for D_b, these authors studied diffusion along triple junctions, finding a diffusivity of $3.4D_b$ for them. We cannot adopt this as the vein diffusivity
210 D_v, because their model does not recognise water-filled veins at triple junctions, whose presence in ice has been confirmed by optical (Mader, 1992a) and nuclear magnetic resonance (Brox et al., 2015) methods.

2.3 Continuum formulation

215 For the system in Fig. 1, let us denote the concentrations of a trace isotope (^{18}O or D) in the ice, vein, and grain boundaries by $N_s(r, \theta, z, t)$, $N_v(z, t)$, and $N_b(r, z, t)$, respectively, where t is time. We assume N_v to be independent of r and θ, and N_b to be uniform across the grain-boundary thickness. The concentrations satisfy the conservation equations

$$\frac{\partial N_s}{\partial t} = D_s \left(\frac{1}{r} \frac{\partial}{\partial r} \left(r \frac{\partial N_s}{\partial r} \right) + \frac{1}{r^2} \frac{\partial^2 N_s}{\partial \theta^2} + \frac{\partial^2 N_s}{\partial z^2} \right) , \tag{3}$$

$$\frac{\partial N_v}{\partial t} = D_v \frac{\partial^2 N_v}{\partial z^2} - w \frac{\partial N_v}{\partial z} + \frac{3D_s}{\pi a} \int_0^L \frac{\partial N_s}{\partial r} \bigg|_{r=a} \mathrm{d}\theta + \frac{3cD_b}{\pi a^2} \frac{\partial N_b}{\partial r} \bigg|_{r=a} , \tag{4}$$

220 $$\frac{\partial N_b}{\partial t} = D_b \left(\frac{\partial^2 N_b}{\partial r^2} + \frac{\partial^2 N_b}{\partial z^2} \right) + \frac{2D_s}{rc} \frac{\partial N_s}{\partial \theta} \bigg|_{\theta=0} , \tag{5}$$

where w is the vein-flow velocity in the downward (z-) direction, and other symbols have been introduced. These equations account for isotopic exchange across the vein wall, between grain boundaries and vein, and between grain boundaries and ice (the last two terms in Eq. (4) and the final term in Eq. (5)). The factor 3 sums contributions to the vein from all directions. Taylor dispersion along the vein is ignored as the corresponding Péclet number ($\lesssim 10^{-1}$) would only raise the vein liquid

225 diffusivity by $< 0.1\%$. We specify the boundary conditions $\partial N_s/\partial r = \partial N_b/\partial r = 0$ at $r = b$ (zero gradient in the interior) and anticipate $\partial N_s/\partial \theta = 0$ at $r = a$, because the vein wall at different azimuths contacts the same vein isotopic concentration. Rotational periodicity implies solution symmetry in $0 \le \theta \le L$ about $L/2$.

Deriving a model for the isotopic deviation δ follows Rempel and Wettlaufer's (2003) method. If N_{s0}, N_{v0} and N_{b0} are the number densities of the major isotope (^{16}O or H) in the three components, then equilibrium fractionation at the vein wall and

230 at the vein-end of grain boundaries yields $\alpha N_v/N_{v0} = N_s|_{r=a}/N_{s0} = N_b|_{r=a}/N_{b0}$, where $\alpha \approx 1$ is the fractionation coefficient. We assume no fractionation on the side-walls of grain boundaries (Sect. 2.2), so $N_b = N_s|_{\theta=0}$ in $r \ge a$. By rewriting Eqs. (4) and (5) in terms of N_s (with $N_{v0} \approx N_{b0} \approx N_{s0}$ taken as constant), eliminating their time derivatives with Eq. (3), and using the definition

$$\delta = \delta(r, \theta, z, t) = \frac{N_s}{N_{s0}} - 1 , \tag{6}$$

we obtain the diffusion equation

235 $$\frac{\partial \delta}{\partial t} = D_s \left(\frac{1}{r} \frac{\partial}{\partial r} \left(r \frac{\partial \delta}{\partial r} \right) + \frac{1}{r^2} \frac{\partial^2 \delta}{\partial \theta^2} + \frac{\partial^2 \delta}{\partial z^2} \right) , \tag{7}$$

with the boundary conditions

$$\frac{\partial \delta}{\partial r} \bigg|_{r=b} = 0 , \quad \frac{\partial \delta}{\partial \theta} \bigg|_{r=a} = 0 , \tag{8}$$

$$\frac{\partial^2 \delta}{\partial r^2} - \beta_v \frac{\partial^2 \delta}{\partial z^2} + \frac{w}{D_s}\frac{\partial \delta}{\partial z} + \frac{1}{a}\left(\frac{\partial \delta}{\partial r} - \frac{3\alpha}{\pi}\int_0^L \frac{\partial \delta}{\partial r}\,d\theta - \frac{3\alpha\varepsilon}{\pi}(\beta_b+1)\frac{\partial \delta}{\partial r}\bigg|_{r=a,\,\theta=0}\right) = 0 \quad \text{at } r = a, \tag{9}$$

$$\frac{1}{r}\frac{\partial \delta}{\partial r} - \beta_b\left(\frac{\partial^2 \delta}{\partial r^2} + \frac{\partial^2 \delta}{\partial z^2}\right) + \frac{1}{r^2}\frac{\partial^2 \delta}{\partial \theta^2} - \frac{2}{rc}\frac{\partial \delta}{\partial \theta} = 0 \quad \text{on } \theta = 0, \; a \le r \le b \tag{10}$$

240 (the analogous boundary condition at $\theta = L$ is automatically met, given the solution symmetry). The boundary conditions in Eqs. (9) and (10) encapsulate advection and diffusion along the vein and diffusion within the grain-boundary planes. We have introduced the thinness parameter

$$\varepsilon = \frac{c}{a} \quad (\ll 1)\,, \tag{11}$$

which measures the grain-boundary thickness scaled to the vein radius. The parameters

245 $$\beta_v = \frac{D_v}{D_s} - 1 \quad \text{and} \quad \beta_b = \frac{D_b}{D_s} - 1 \tag{12}$$

quantify the diffusivity contrasts of water to ice and grain boundary to ice, respectively. As noted in Sect. 2.2, typically $\beta_v \sim 10^6$ (Fig. 2); β_b ($< \beta_v$) is also large, but depends on the chosen grain-boundary diffusivity. Notice one cannot lump all grain-boundary properties into a single parameter (e.g. the diffusivity–thickness product cD_b or $\varepsilon(\beta_b + 1)$) in this model.

The partial differential equation problem for δ in Eqs. (7) to (10) is linear. To quantify signal decay, we follow the past 250 theories and study how sinusoidal signals of different wavelength λ (or wavenumber $k_z = 2\pi/\lambda$) smooth out in time by posing the trial solution

$$\delta \propto H(r,\theta)\exp(-D_s\zeta t + ik_z z)\,, \tag{13}$$

where $\zeta = \zeta_R + i\zeta_I$ is a complex decay-rate parameter. The enhancement factor measuring the level of excess diffusion is given by the ratio of the signal decay rate $D_s\zeta_R$ in Eq. (13) to the baseline decay rate $D_s k_z^2$ in monocrystalline ice (ice without grain boundaries and veins). On defining $\zeta_R = k_z^2 + k_r^2$, the enhancement factor is

$$f = 1 + \frac{k_r^2}{k_z^2}\,. \tag{14}$$

In Eq. (13), the function $H(r, \theta) = H_R + iH_I$ determines the spatial pattern of isotopic signals in three dimensions (3D). At depth z, $Re[H\exp(ik_z z)]$ gives their amplitude across the annular sector $0 \le \theta \le L$, $a \le r \le b$, and the section-mean isotopic signal (ignoring the exponential time decay factor) is

260 $$3\int_0^L \int_a^b Re[rH(r,\theta)\exp(-ik_z z)]\,dr\,d\theta\,. \tag{15}$$

The phase angle $\phi = \tan^{-1}(H_I/H_R) + k_z z - D_s\zeta_I t$ of the signals shows that they migrate downward at the velocity $\zeta_I D_s/k_z$.

2.4 *Scaled model*

When addressing isotopic patterns later, it will be useful to reference the features on them (e.g. size or radial position) to the

265 grain radius b. To facilitate this, we non-dimensionalise the model by letting

$$r* = \frac{r}{b} , \tag{16}$$

at the same time scaling other variables as follows:

$$z* = \frac{z}{b} , \quad t* = \frac{t}{(b^2/D_s)} , \quad \lambda* = \frac{\lambda}{b} , \quad \zeta* = b^2\zeta , \quad [k_z*, k_r*] = b[k_z, k_r] . \tag{17}$$

The scaled model equivalent to Eqs. (7) to (10) is then

270 $$\frac{\partial \delta}{\partial t} = \frac{1}{r}\frac{\partial}{\partial r}\left(r\frac{\partial \delta}{\partial r}\right) + \frac{1}{r^2}\frac{\partial^2 \delta}{\partial \theta^2} + \frac{\partial^2 \delta}{\partial z^2} , \tag{18a}$$

$$\partial\delta/\partial r\big|_{r=1} = 0 , \quad \partial\delta/\partial\theta\big|_{r=\xi} = 0 , \tag{18b}$$

$$\frac{\partial^2 \delta}{\partial r^2} - \beta_v \frac{\partial^2 \delta}{\partial z^2} + \chi\frac{\partial \delta}{\partial z} + \frac{1}{\xi}\left(\frac{\partial \delta}{\partial r} - \frac{3\alpha}{\pi}\int_0^L \frac{\partial \delta}{\partial r}\,d\theta - \frac{3\alpha\varepsilon}{\pi}(\beta_b+1)\frac{\partial \delta}{\partial r}\bigg|_{r=a,\,\theta=0}\right) = 0 \quad \text{at} \quad r = \xi , \tag{18c}$$

$$\frac{1}{r}\frac{\partial \delta}{\partial r} - \beta_b\left(\frac{\partial^2 \delta}{\partial r^2} + \frac{\partial^2 \delta}{\partial z^2}\right) + \frac{1}{r^2}\frac{\partial^2 \delta}{\partial \theta^2} - \frac{2}{r(\varepsilon\xi)}\frac{\partial \delta}{\partial \theta} = 0 \quad \text{on} \quad \theta = 0 , \tag{18d}$$

where we have dropped the stars for convenience (we work with dimensionless variables from now on). The parameter

275 $$\xi = \frac{a}{b} \quad (\ll 1) \tag{19}$$

is the dimensionless vein radius ($c \ll a \ll b$ in glacier ice translates to $\varepsilon\xi \ll \xi \ll 1$), and

$$\chi = \frac{wb}{D_s} \tag{20}$$

is a Péclet number measuring the importance of vein-flow driven advection relative to solid-state diffusion. The trial solution in Eq. (13) becomes

280 $$\delta \propto H(r,\theta)\exp(-\zeta t + ik_z z) , \tag{21}$$

while Eq. (14) for the enhancement factor f is unchanged under the scaling.

2.5 *Eigenvalue problem*

It remains to solve for the pattern $H(r, \theta)$ for signals of any wavenumber k_z. Substituting δ from Eq. (21) into Eq. (18) leads to

$$\frac{\partial^2 H}{\partial r^2} + \frac{1}{r}\frac{\partial H}{\partial r} + \frac{1}{r^2}\frac{\partial^2 H}{\partial \theta^2} + s^2 H = 0 \,, \tag{22}$$

with the boundary conditions

$$\left.\partial H/\partial r\right|_{r=1} = 0 \,, \quad \left.\partial H/\partial \theta\right|_{r=\xi} = 0 \,, \tag{23}$$

$$\left.\frac{\partial^2 H}{\partial r^2}\right|_{r=\xi} + p_1 H\big|_{r=\xi} + \frac{1}{\xi}\left(\left.\frac{\partial H}{\partial r}\right|_{r=\xi} - \frac{p_2}{L}\int_0^L \left.\frac{\partial H}{\partial r}\right|_{r=\xi}\,\mathrm{d}\theta - \frac{p_3}{L}\left.\frac{\partial H}{\partial r}\right|_{r=\xi,\,\theta=0}\right) = 0 \,, \tag{24}$$

$$\left.\frac{1}{r}\frac{\partial H}{\partial r}\right|_{\theta=0} - \beta_{\mathrm{b}}\left(\left.\frac{\partial^2 H}{\partial r^2}\right|_{\theta=0} - k_z^{\,2} H\big|_{\theta=0}\right) + \left.\frac{1}{r^2}\frac{\partial^2 H}{\partial \theta^2}\right|_{\theta=0} - \frac{2}{r(\varepsilon\xi)}\left.\frac{\partial H}{\partial \theta}\right|_{\theta=0} = 0 \,. \tag{25}$$

Here, we have defined

$$s^2 = k_r^{\,2} + i\zeta_I \tag{26}$$

and introduced the parameters

$$p_1 = \beta_{\mathrm{v}} k_z^{\,2} + ik_z\chi, \quad p_2 = 2\alpha, \quad p_3 = 2\alpha\varepsilon(\beta_{\mathrm{b}} + 1) \,. \tag{27}$$

Eqs. (24) and (25) may be further simplified by using Eq. (22) to reduce the number of high-order derivatives; thus, we find

$$\left.(p_1 - s^2) H\right|_{r=\xi} = \frac{1}{\xi L}\left(p_2 \int_0^L \left.\frac{\partial H}{\partial r}\right|_{r=\xi}\,\mathrm{d}\theta + p_3 \left.\frac{\partial H}{\partial r}\right|_{r=\xi,\,\theta=0}\right) \tag{28}$$

and

$$\left.\frac{\partial^2 H}{\partial r^2}\right|_{\theta=0} - \frac{\beta_{\mathrm{b}} k_z^{\,2} - s^2}{\beta_{\mathrm{b}} + 1} H\big|_{\theta=0} = -\frac{2}{(\beta_{\mathrm{b}} + 1)r\varepsilon\xi}\left.\frac{\partial H}{\partial \theta}\right|_{\theta=0} \,. \tag{29}$$

Eqs. (22), (23), (28) and (29) need to be solved to determine the isotopic patterns. They constitute a homogeneous boundary value problem for H with the eigenvalue s^2, whose imaginary part ζ_I is non-zero if the vein-water flows (w, $\chi \neq 0$). The slowest-decaying eigenmode (with minimum $\mathrm{Re}(s^2) > 0$) yields the desired pattern. The problem is non-trivial because of mixed boundary conditions at the vein wall and the grain boundaries. Solution by the separation of variables $H = H_1(r)H_2(\theta)$ can exploit the periodicity in θ for H_2; equivalently, one can take the cosine transform azimuthally (e.g. $\sqrt{2/L}\int_0^L H\cos(n\theta/L)\mathrm{d}\theta$) and the Hankel transform in the radial direction. However, we find that analytic solution does not seem feasible by these conventional approaches – a fundamental obstacle being mismatch between the Fourier kernel of the grain-boundary condition in Eq. (29) and the Hankel kernel of the differential operator in Eq. (22). We therefore solve the problem numerically. Readers not interested in the associated details (Sect. 2.6) might skip on to Sect. 3.

2.6 *Numerical method*

We use the pseudo-spectral method, employing Chebyshev collocation in the θ-direction to achieve "spectral accuracy" in

310 approximating the solution (Boyd, 2000; Trethethen, 2000). Although the angular periodicity suggests using trigonometric basis functions instead (i.e. Fourier spectral method), the corresponding approximation lacks spectral accuracy and converges much more slowly than Chebyshev polynomials, as H is nonsmooth (with discontinuous gradient) across the grain boundaries. We use the finite-difference approximation in the radial direction.

The solution on each grain boundary can be written as $G(r) \equiv H(r, 0)$. This enables us to work with alternative variables,

315 by splitting H into the sum

$$H(r,\theta) = F(r,\theta) + G(r) \,, \tag{30}$$

where the field F represents variations in the ice sector not accounted for by G. Usefully, F is zero along the grain boundaries and on the vein wall (as $\partial H/\partial\theta = 0$ there). The decomposition converts Eqs. (22) and (23) to the partial differential equation

$$F_{rr} + \frac{F_r}{r} + \frac{F_{\theta\theta}}{r^2} + s^2 F = -(G'' + \frac{G'}{r} + s^2 G) \tag{31}$$

320 with the homogeneous boundary conditions

$$F_r\big|_{r=1} = 0 \,, \qquad F(r,\ 0) = F(r,\ L) = 0 \,, \qquad F(\xi,\ \theta) = 0 \,. \tag{32}$$

Meanwhile, Eqs. (29) and (28) become the ordinary differential equation

$$G'' - \frac{\beta_b k_z^2 - s^2}{\beta_b + 1} G = -\frac{2}{(\beta_b + 1)r\varepsilon\xi} F_\theta\big|_{\theta=0} \,, \tag{33}$$

with boundary conditions (BC's) at the vein wall and in the grain interior given by

325 $$(p_1 - s^2)G(\xi) = \frac{1}{\xi}\left[\frac{p_2}{L}\int_0^L F_r\big|_{r=\xi}\mathrm{d}\theta + \left(p_2 + \frac{p_3}{L}\right)G'(\xi)\right] \tag{34}$$

$$G'(1) = 0 \,. \tag{35}$$

We have used the prime (/subscript) notation to denote ordinary (/partial) derivatives above. The differential equations for G and F are coupled via their source terms.

Because the vein short-circuits diffusion in the ice, we expect the solution to vary rapidly just outside the vein wall and

330 slowly in the grain interior, notably away from grain boundaries. To resolve the variations near $r = \xi$ (vein wall) with sufficient grid points, without over-introducing grid points in the interior (which slows numerical computation), we make a change of the radial variable

$$R = 1 - \ln r \,, \quad \text{i.e.,} \quad r = e^{-(R-1)} \,. \tag{36}$$

The interior and the vein wall are located at $R = 1$ and $R = R_{\max} = 1 - \ln\xi$, respectively (Fig. 3a).
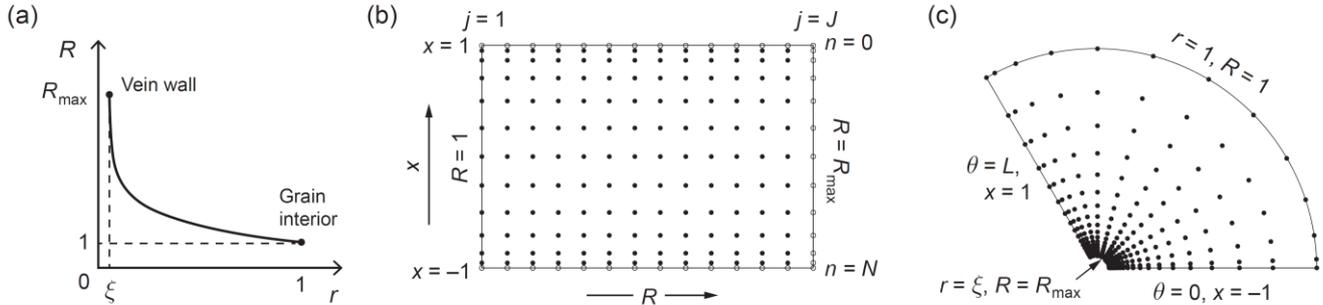
Figure 3. Elements of the mixed spectral–finite difference numerical method. (a) Radial coordinate transformation used to increase spatial resolution near the vein. (b) Numerical grid for $F(R, x)$. Filled dots indicate solution points; open circles, zero boundary values. (c) The same grid points on the ice domain. Panels (b) and (c) are illustrative; we use many more grid points ($N = 100$, $J = 201$) than shown.

Next, we set up the Chebyshev collocation points

$$x = \cos\left(\frac{n\pi}{N}\right), \quad n = 0, 1, 2 \ldots, N, \tag{37}$$

choosing

$$\theta = \frac{L}{2}(x+1) \tag{38}$$

such that the interval $x = [-1, 1]$ maps onto the angular range $\theta = [0, L]$ of the sector (Fig. 3b, c). With these transformations, the coupled problem for F and G becomes

$$-e^{2(R-1)}\left[F_{RR} + \left(\frac{2}{L}\right)^2 F_{xx}\right] + e^{2(R-1)}\left[\beta_b G'' + (\beta_b + 1)G'\right] - \beta_b k_z^2 G + \frac{4e^{R-1}}{(\varepsilon\xi)L}F_x\big|_{x=-1} = s^2 F, \tag{39a}$$

$$\text{BC's:} \quad F_R\big|_{R=1} = 0, \quad F(R, x=\pm 1) = 0, \quad F(R_{\max}, x) = 0, \tag{39b}$$

and

$$-(\beta_b + 1)e^{2(R-1)}(G'' + G') + \beta_b k_z^2 G - \frac{4e^{R-1}}{(\varepsilon\xi)L}F_x\big|_{x=-1} = s^2 G, \tag{40a}$$

$$\text{BC's:} \quad \frac{1}{\xi^2}\left[\frac{p_2}{2}\int_{-1}^{1} F_R\big|_{R=R_{\max}} \mathrm{d}x + \left(p_2 + \frac{p_3}{L}\right)G'(R_{\max})\right] + p_1 G(R_{\max}) = s^2 G(R_{\max}), \quad G'(1) = 0. \tag{40b}$$

We have written these results with s^2 on the right-hand side to facilitate the eigenvalue calculation.

The method proceeds by discretising the x-axis with the Chebyshev points and the R-axis as J equidistant points (Fig. 3b) and using the spectral differentiation matrix of Trefethen (2000; p.53) and finite differencing to compute derivatives in these respective directions. With F zero on three edges of the solution domain, there are $(N-1)(J-1)$ unknowns in $F_{n,j}$ and J unknowns

355 in G_j, for $n = 0, 1, 2 \ldots, N$ and $j = 1, 2 \ldots, J$. The scheme converts Eqs. (39) and (40) into a system of linear equations $\mathbf{Mv} = s^2\mathbf{v}$, where the solution eigenvector (a column vector)

$$\mathbf{v} = [\; F_{1,1}\; F_{1,2} \ldots F_{1,J–1} \quad F_{2,1}\; F_{2,2} \ldots F_{2,J–1} \quad F_{3,1}\; F_{3,2} \ldots F_{3,J–1} \quad \ldots \quad F_{N–1,1}\; F_{N–1,2} \ldots F_{N–1,J–1} \quad G_1\; G_2 \ldots G_J \;]^T \quad (41)$$

has $(N–1)(J–1) + J$ elements, and $\mathbf{M}$ is a sparse-banded matrix (detailed in Section S1 and Fig. S1 in the Supplement). After using the MATLAB function eig to compute s^2 from $\mathbf{M}$, we find $\mathbf{v}$ corresponding to the slowest-decaying eigenmode and put

360 $F_{n,j}$ and G_j back in cylindrical polar coordinates to build the solution H. Our computation used $N = 100$ and $J = 201$, and we checked for numerical convergence and convergence at small c towards Ng's (2023) analytic solution (for the vein-only system without grain boundaries). All isotopic patterns reported below display H after it has been regridded at a constant θ-spacing by Lagrange interpolation from the Chebyshev grid values, normalised by the value of H at $r = 1$, $\theta = L/2$ in the grain interior, and copied from $0 \leq \theta \leq L$ into the other sectors to fill the ice annulus.

365 ## 3 Results and analysis

We proceed to examine computed isotopic patterns (Sect. 3.1) and bulk-diffusivity enhancement factors (Sect. 3.2) for different model parameters. In our model runs, we set the vein and grain sizes at $a = 1$ µm and $b = 1$ mm and assume the fractionation coefficient $\alpha = 1$, so the results can be compared with those of Rempel and Wettlaufer (2003) and Ng (2023) and applied to either δ^{18}O or δD. Using precise fractionation coefficients (≈ 1.003 for oxygen, ≈ 1.02 for hydrogen) changes the results

370 numerically in a minor way that does not alter our qualitative findings.

There are 30 parameter combinations from the choices of temperatures (–32 °C, –52 °C), grain-boundary diffusivities (Table 1), and grain-boundary thicknesses ($c = 1, 5, 10$ nm). For each combination, we compute results for signal wavelengths λ across the range 0.005–0.15 m and different vein-water flow velocities w in 0–50 m yr^{-1} when $T = –32$ °C and 0–5 m yr^{-1} when –52 °C. We analyse selected runs below to highlight the effect of grain-scale short-circuiting on the isotopic patterns.

375 For ease of describing grain-boundary properties, we refer to the choices of D_b at each temperature as *low*, *medium-low*, *medium*, *medium-high*, and *high* (see descriptive scale in Fig. 2) and the choices of c as *thin*, *intermediate*, and *thick*. Not all combinations will be analysed below (e.g. not the patterns for medium-low D_b, which typically resemble and fall between the low and medium cases). As we shall see, the more interesting pattern transitions occur as D_b varies from medium to high.

380 ### 3.1 *Isotopic patterns in 3D*

Figure 4 shows the predicted patterns at $T = –32$ °C, $\lambda = 2$ cm, and $w = 0$, for three runs with intermediate (5 nm thick) grain boundaries having high, medium-high and medium diffusivities. They illustrate the change from an axisymmetric "pole" pattern to a "3-spoke" pattern as D_b increases, which is one of our key findings. In each panel, the colour charts show variations

in δ – i.e. $Re[H(r, \theta)\exp(ik_z z)]$ after normalisation by $H(1, L/2)$ (Sects. 2.3 & 2.6) – at three depths in the range spanning 1λ.

385 We are looking down the cylindrical domain in Fig. 1a and taking horizontal slices of its isotopic deviation, analogous to cuts perpendicular to a vertical triple junction in ice. The far-left plot shows the depth profiles of isotopic variations in the grain interior ($r = 1$, $\theta = L/2$; black curve) and grain-boundary interior ($r = 1$, $\theta = 0$; blue) and along the vein (red). To emphasise where fast changes occur on each pattern, the colour scale is always fitted to its maximal range of variations, and we use one of two colour schemes depending on whether δ at the vein is higher or lower than δ in the interior. Note that the isotopic signals

390 decay in time following Eqs. (13) and (21), and the patterns occur on a background (mean) isotopic concentration that would first be subtracted when studying real ice samples.
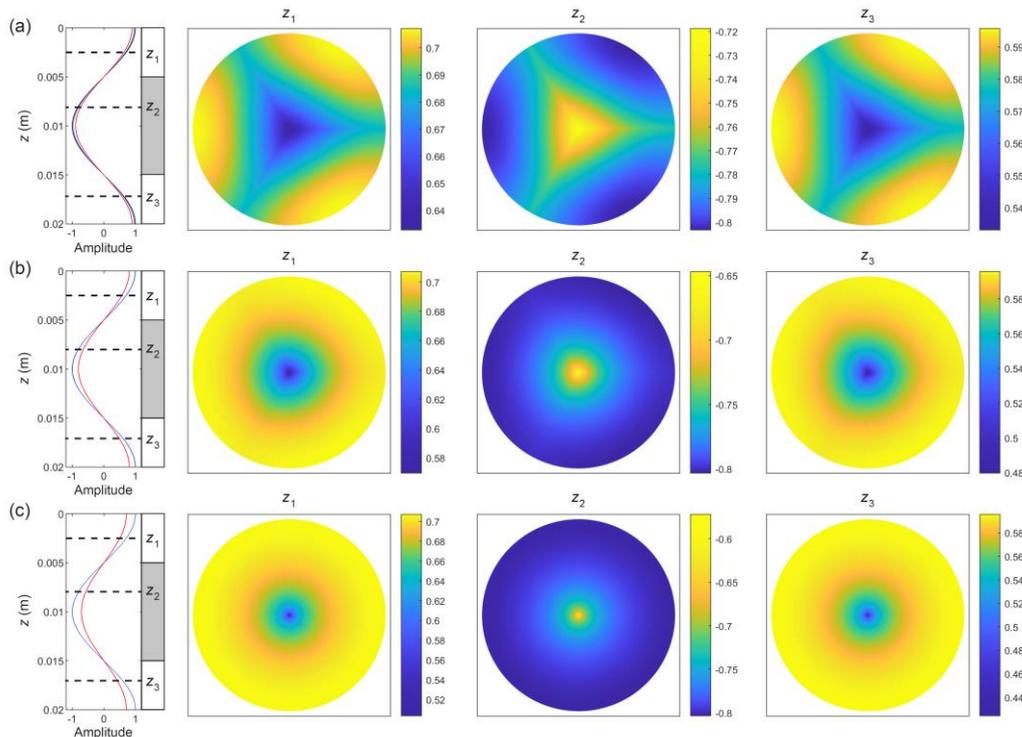
Figure 4. Horizontal isotopic patterns computed in three model runs with $T = -32$ °C, $\lambda = 2$ cm, $c = 5$ nm, $w = 0$ m yr^{-1}, and D_b = (a) $1.5 \times$

395 10^{-11} m^2 s^{-1}, (b) 1.5×10^{-12} m^2 s^{-1}, (c) 1.5×10^{-13} m^2 s^{-1}, compiled by sampling the normalised δ-variations in the annular domain of Fig. 1a at three depths (z_1, z_2, z_3). The colour charts reach out to the ice grain radius; the vein at centre is too small to be visible. One of two colour schemes is used, depending on whether δ at the vein exceeds δ in the grain interior or vice versa. At far left in each panel, the curves show the depth profiles of the δ-variations at three sites – mid-grain interior (black), grain-boundary interior (blue), and vein wall (red) – over a signal wavelength (note that the black curves in (b) and (c) are overlain by the blue.) White and grey bars indicate vertical stretches where

400 the vein-versus-interior difference in δ has the same sign. The enhancement factors in these runs are $f = 3.22$, 2.42, and 2.20, respectively.

First we analyse Fig. 4b – the medium-high diffusivity run – to explain salient features and how the patterns relate to the short-circuiting. This solution shows what the axisymmetric theories (Nye, 1998; Rempel and Wettlaufer, 2003; Ng, 2023) predict, with isotopes diffusing radially towards the vein (e.g. at $z = z_1, z_3$), up and down along the vein, and back into ice and radially outwards (z_2). As in those theories, these exchanges bypass slow solid diffusion in the ice to cause excess diffusion

405 and accelerates the signal decay – the computed enhancement factor f is 2.42 (> 1) – and they induce radial variations in δ that are the most rapid immediately outside the vein. These δ-excursions cause the pole (z_2) and hole (z_1, z_3) patterns, which respectively reflect the role of the vein as a source and sink of isotopes in different horizontal sections in the short-circuiting.

The vertical stretches where isotopes diffuse radially inwards and outwards are identified by where δ in the ice exceeds δ in the vein and vice versa, as indicated by boxes by the far-left plot. In each stretch, the patterns' strength (magnitude of their

410 horizontal isotopic variations) varies with depth according to the difference in δ between the vein and interior. But the patterns themselves hardly change with depth except very near the stretch transitions. This near-invariance arises because $\lambda \gg b$, so that, away from the transitions, vertical gradients in δ are much smaller than horizontal gradients in the system, and the diffusion problems determining the pattern at different depths are similar[2]. At the transitions, where the vein-to-interior difference in δ switches sign, the pattern flips from a pole to a hole or the other way. Movie S1 shows the complete pattern

415 evolution over 1λ. The stable "archetypal patterns" in the two stretches are paired, with the same form but oppositely signed, so hereafter we write "pole" for both poles and holes. Detailed examination shows that within a narrow distance about each transition, the pattern evolves continuously, with a pole weakening to zero strength and reversing sign. This behaviour is not resolved in Movie S1 but can be gauged from its dynamic colour ranges.

The poles in Fig. 4b are not axisymmetric: they exhibit deformities reflecting the grain boundaries, whose impression is
420 faint in this case. In contrast, Fig. 4a (high-diffusivity run, where D_b is ten-fold) shows a much stronger grain-boundary imprint that causes 3-spoke patterns. Here, the vein plays a similar role in the short-circuiting as before; the archetypal patterns again flip across transitions. But isotopes also diffuse from the ice to grain boundaries and along them to the vein (vice versa at other depths), and diffusion occurs vertically within the grain boundaries. Fast diffusion along them extend the poles to form the spokes and cause extra short-circuiting across the ice-crystal sectors, which raises the excess diffusion ($f = 3.22$). The 3D

425 isotopic field is more complex than in the run of Fig. 4b. Azimuthal variations are evident from the spoke patterns and the δ-difference between the ice interior and grain-boundary interior (black and blue curves, Fig. 4a). The strongest azimuthal

---

[2] Mathematically, $\lambda \gg b$ (dimensionally) translates to $k_z \ll 1$ and $p_1 \ll 1$ in the scaled model of Sects. 2.4 and 2.5, so that Eqs. (22) to (25) for H approximate a boundary value problem with terms representing vertical gradients neglected. Near the transitions, this approximation does not hold because $H \approx 0$ and those terms become comparable to the radial and azimuthal gradients.
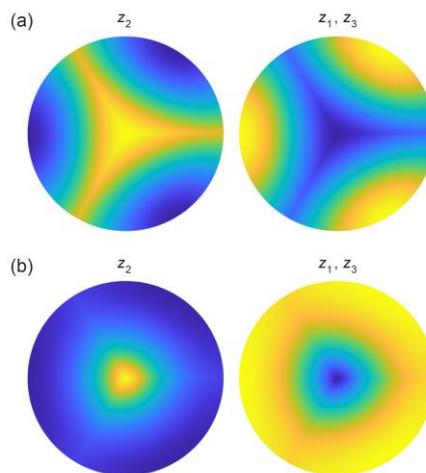
Figure 5. Archetypal isotopic patterns computed in two model runs assuming $T = -32$ °C, $\lambda = 2$ cm, $c = 10$ nm, $w = 0$ m yr^{-1}, and $D_b = $ (a)

430   1.5×10^{-11} m^2 s^{-1} and (b) 1.5×10^{-12} m^2 s^{-1}, sampled at the same depths as those in Fig. 4 (z_1, z_2, and z_3), and shown with the scheme used there. The enhancement factors in these runs are $f = 3.93$ and 2.55, respectively.

gradients occur just outside the vein on either side of grain boundaries, so lateral short-circuiting dominates near each ice sector's apex. The increased short-circuiting also reduces the vein-to-interior difference in δ, compared to the last run.

435   Going the other way, lowering D_b to medium diffusivity (Fig. 4c) suppresses the grain-boundary imprint and shrinks the poles, which still show corners but only at tiny radius. These changes are expected given the diminishing short-circuiting contribution of the grain boundaries. Indeed, this solution (with $f = 2.20$) approximates the axisymmetric solution of Rempel and Wettlaufer (2003) and Ng (2023), where $f = 2.11$ in the absence of grain boundaries under the same conditions (see Ng's Fig. 3a). Their solution is approached even more closely if we reduce D_b to medium-low or low, towards the solid diffusivity

440   D_s. For the interested reader, Movies S2 and S3 document the depth-evolving isotopic patterns in the runs of Fig. 4a and 4c.

Next we vary the grain boundary thickness c. Fig. 5 presents archetypal patterns in two runs at -32 °C assuming thick grain boundaries ($c = 10$ nm) of high and medium-high diffusivities. Compared to the runs in Fig. 4a and b, which used the same D_b values, these patterns have more developed grain-boundary imprints and enlarged central excursions, and the associated enhancement factors are higher. As expected, thickening the grain boundaries here has a similar effect as raising D_b

445   in terms of enhancing grain-boundary short-circuiting, so the transition from a pole to 3-spoke pattern occurs at lower diffusivity. We experimented also with thin grain boundaries ($c = 1$ nm), finding that this shifts the pole-to-spoke transition to higher diffusivity instead. The corresponding archetypal patterns feature in Fig. 10 described later.

All experiments so far assume no vein-water flow, so their vertical isotopic variations at different positions (r, θ) have identical phase, $\phi = 0$ (Fig. 4, curves). What if $w \neq 0$? Fig. 6 shows the results of four runs assuming intermediate and thick

450   grain-boundaries with high and medium-high diffusivities, where we set w to 5 m yr^{-1}, leaving other parameters unchanged.

Ng (2023) explained that vein-water flow displaces the vein signal against the interior signal to induce a "shear layer" of phase-shifted isotopic variations outside the vein wall. In turn, the shear layer generates strong radial gradients in isotopic concentration in the ice near the vein, amplifying the diffusive isotope exchange between ice and vein to raise the level of excess diffusion. Fig. 6 shows the vein signal displaced in all four runs. Each solution still has two transitions and paired archetypal patterns in two stretches of equal length, within 1λ. Fig. 7 depicts the shear layer on a map of ϕ for the run in Fig. 6a, showing also the radial transects of H at $\theta = 0$ and $L/2$. A non-zero imaginary part to H implies a phase shift that reaches $-15°$ by the vein in this run. Unlike in Ng's (axisymmetric) theory, the shear layer here is triangular (non-circular) in planform due to lateral short-circuiting by the grain-boundaries, so isotopic transport in 3D is complicated by both vein-water flow and the grain boundaries' presence. All four experiments confirm the amplification of excess diffusion by w anticipated by Ng's study: f is higher than in the runs where $w = 0$ (cf. Figs. 4a–b and 5). Actually, their archetypal patterns closely resemble the ones found earlier, because the vein-flow induced shear layer causes only subtle changes to them (cf. Figs. 4a, b & 5), but the phase shifts between the vein and interior signals increase the amplitude difference between these signals at most depths, and so markedly strengthen the patterns (e.g. curves in Fig. 6a, b; cf. Fig. 4a, b). Vein-water flow thus makes the patterns easier to detect, even though it affects their form only in minor ways.
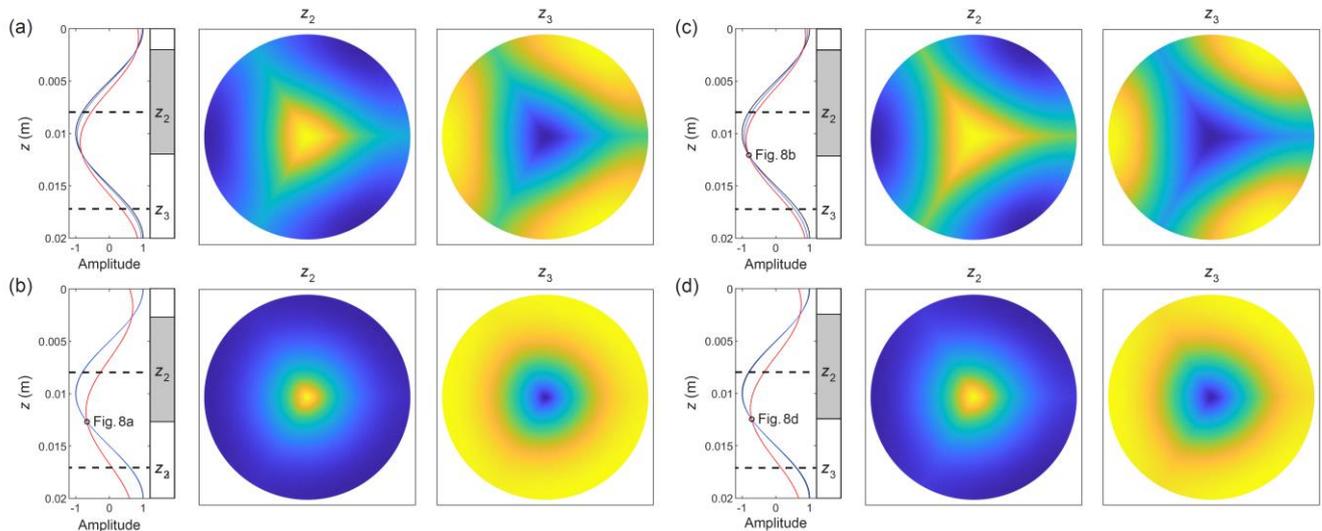
Figure 6. Archetypal isotopic patterns computed in four runs with $T = -32$ °C, $\lambda = 2$ cm, $w = 5$ m yr^{-1} (downward vein-water flow), and the grain-boundary properties (a) $D_b = 1.5 \times 10^{-11}$ m^2 s^{-1}, $c = 5$ nm; (b) $D_b = 1.5 \times 10^{-12}$ m^2 s^{-1}, $c = 5$ nm; (c) $D_b = 1.5 \times 10^{-11}$ m^2 s^{-1}, $c = 10$ nm; (d) $D_b = 1.5 \times 10^{-12}$ m^2 s^{-1}, $c = 10$ nm. The layout of Fig. 4 is used here, but only the depths z_2 and z_3 are sampled, and we omit the colour range on each pattern, which is defined by the difference between the vertical isotopic profiles (curves at far left) for the mid-grain interior (black), grain-boundary interior (blue), and vein wall (red). The enhancement factors in these runs are $f = $ (a) 4.13, (b) 3.86 [cf. $f = 3.24$ in Fig. 3b of Ng (2023), which he found for the same conditions in the model without grain boundaries], (c) 4.61, and (d) 3.92.
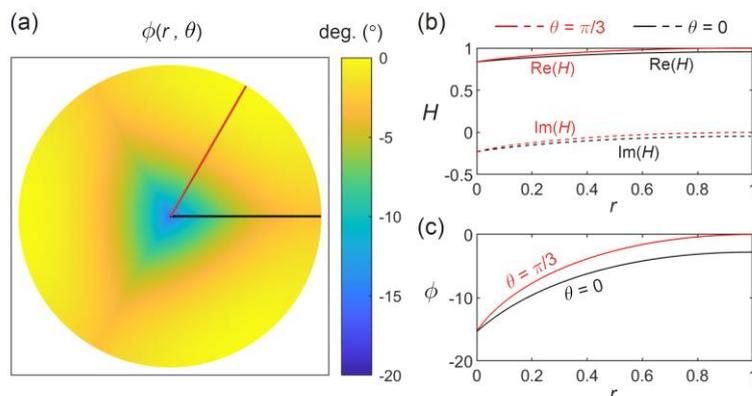
Figure 7. (a) Map of phase angle ϕ for the experiment of Fig. 6a. (b, c) Corresponding radial transects of the solution H and ϕ along $\theta = 0$ (black; i.e. grain boundary) and $\theta = \pi/3$ or $L/2$ (red). Location lines in (a) use the same colour coding.

When $w \neq 0$, the phase variations also cause unusual patterns to appear in the narrow transitions where each archetypal pattern (hole or spoke type) evolves to its opposite form. Fig. 8 shows examples of these patterns, taken from the last runs and an extra run assuming medium D_b. They include "wheels" with notable azimuthal variations mid-way along grain boundaries (near $\theta = 0$, L, and $2L$ at $r \approx 1$) and "halos" where isotopic concentration varies with radius non-monotonically. Although we mention them for completeness, we expect to see them rarely in measurements, because their small amplitudes probably fall below the measurement sensitivity and the sampling has to be made at precisely the right depth against the bulk signal.
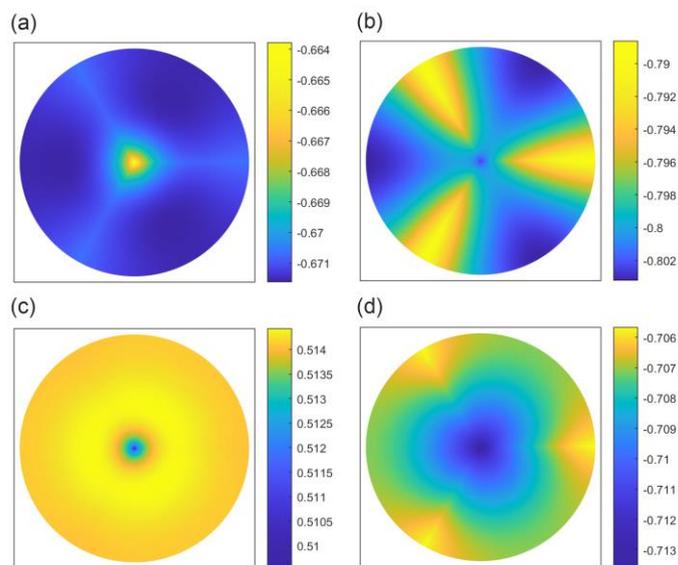
Figure 8. Transitory isotopic patterns from (a, b, d) three of the runs in Fig. 6 (see reference labels there) and (c) a run with $T = -32$ °C, $\lambda = 2$ cm, $w = 5$ m yr^{-1}, $c = 5$ nm, and $D_b = 1.5 \times 10^{-13}$ m^2 s^{-1}. These patterns have low amplitudes because they occur near transition points.
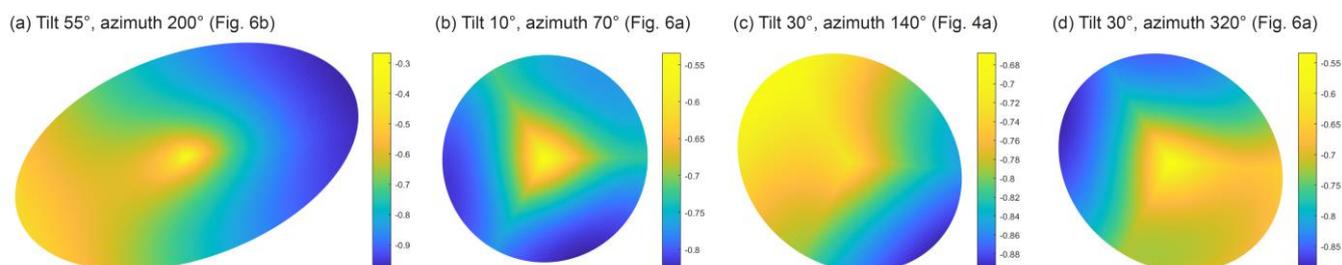
490

Figure 9. Isotopic patterns compiled by sampling several solutions in Figs. 4 and 6 at non-zero tilt from the horizontal (constant z in our model), with the sampled sections meeting $z = z_2$ at $r = 0$. The tilt angle, tilt-axis azimuth and model run are indicated in each case.

Surface and thin sections on real ice will often cross triple junctions at oblique angles to their axes, yielding distorted

495   isotopic patterns for them. Fig. 9 exemplifies potential patterns that may result, made by sampling the solutions in Figs. 4a and 6a–b at tilts of 10°, 30°, and 55° from the horizontal (Movies S4–S7 show how they evolve as the azimuth of the section-normal varies). While this examination stretches our use of an idealised model geometry that ignores the irregular shape of real grain boundaries and triple junctions (e.g. neighbouring junctions in real ice typically differ in orientation), the examples suggest that some pole and spokes may still have visible impressions at moderate tilt. Generally though, only some triple

500   junctions on a given section may show archetypal patterns or their distorted relatives.

Returning to the archetypal patterns, we summarise and elaborate on the insights gained so far on them with the aid of Fig. 10, which puts them on the c–D_b parameter space. The pattern type depends on the relative amount of vein and grain-boundary short-circuiting. Thin, non-diffusive grain-boundaries give a pole pattern, since the short-circuiting is done mostly by the vein. The axisymmetric solution is reproduced at the no-grain-boundary limit $c \to 0$ (dimensionlessly, $\varepsilon \to 0$) or when

505     $D_b \to D_s$ (grain boundaries having the solid diffusivity; $\beta_b \to 0$). Thick, diffusive grain boundaries give 3-spoke patterns, as they serve as radial extensions of the vein in the 3D isotopic exchange; the higher is c or D_b, the more developed are the spokes. The pole-to-spoke transition at –32 °C occurs roughly at medium-high D_b – higher if the grain boundary is thinner. Fig. 10 also indicates that a ten-fold increase in c or D_b leads to what looks like the same pattern, suggesting the thickess–diffusivity product entirely determines the pattern. However, our model analysis (Sect. 3.2) shows that cD_b (or $\varepsilon(\beta_b + 1)$) isn't the sole

510   control; c and D_b also act independently, which is why the ten-fold increases do not give identical enhancement factors.

How about other temperatures? Calculations at –52 °C for 2-cm long signals reveal a similar array of archetypal pole and spoke patterns on the parameter space (Fig. 11; cf. Fig. 10). Vein-water flow again modifies these patterns slightly (Fig. S2) but increases their amplitude and detectability strongly (we find this at other temperatures). That the pattern arrays for –52 and –32 °C bear close resemblance is unsurprising, because the diffusivity contrast $\beta_b = D_b/D_s - 1$ determines the pattern at each
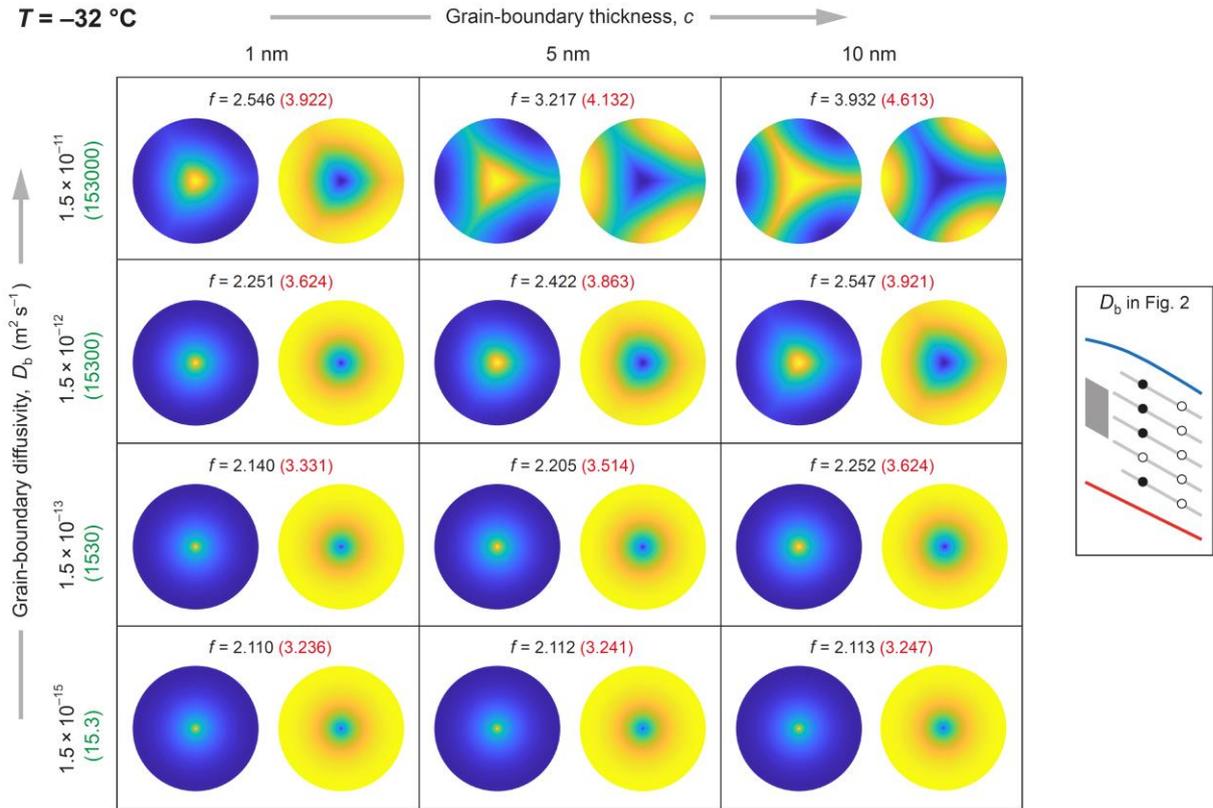
515

Figure 10. Dependence of archetypal patterns on grain-boundary diffusivity D_b and thickness c at –32 °C for signals with the wavelength λ = 2 cm. Key on the right locates the four values of D_b as black filled circles on the scheme of Fig. 2. Numbers in green give the corresponding diffusivity contrasts β_b. The isotopic patterns shown and the enhancement factors f in black are for $w = 0$. Bracketed in red also are the f-values when vein water flows at $w = 5$ m yr^{-1}, which produces patterns that are only slightly different from the ones shown (e.g. Fig. 6).

520

thickness c, and because our D_b values for the two temperatures lie at similar distances above the solid-diffusivity curve (Fig. 2) and convert to similar β_b values (Figs. 10 and 11). The liquid diffusivity D_v also influences the patterns, but β_v varies weakly with T, as $D_v(T)$ and $D_s(T)$ have similar Arrhenius slopes (Fig. 2). These considerations mean that we can predict the isotopic pattern at any temperature from D_b and c, by calculating β_b – or gauging it with Fig. 2 – and then consulting the arrays in Figs.

525 10 and 11. For example, at –42 °C, for grain-boundaries with $D_b = 10^{-14}$ m^2 s^{-1}, Eqs. (1) and (12) give $\beta_b \approx 400$, while in Fig. 2 these T–D_b data plot low on the grey band extrapolated to –42 °C (i.e. extension of the Lu et al. (2009) diffusivity range; Sect. 2.2). Both evaluations put the grain-boundary diffusivity between medium-low and medium on our scale, below the third row of patterns in Figs. 10 and 11, so we predict a pole pattern (regardless of the grain-boundary thickness). An interesting corollary is that isotopic patterns observed in real ice can be used to infer grain-boundary properties (Sect. 4.1).
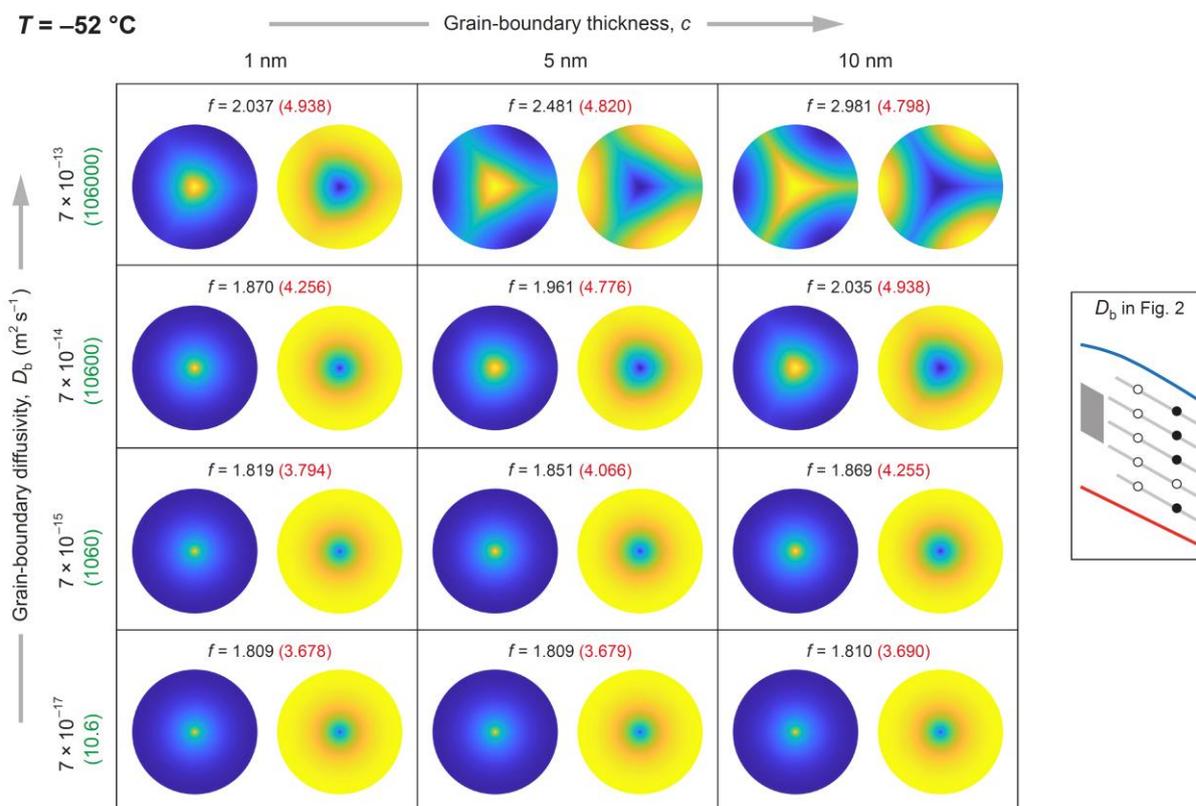
Figure 11. Dependence of archetypal patterns on D_b and c at $T = -52$ °C and $\lambda = 2$ cm. The layout of Fig. 10 is used here. The isotopic patterns shown and the enhancement factors f in black are for $w = 0$. Bracketed in red also are the f-values for vein-water flow at $w = 0.5$ m yr^{-1}, which produces patterns that are only slightly different from the ones shown (Fig. S2).

Hitherto, we have focussed on using the results at $\lambda = 2$ cm to elucidate underlying interactions and pattern controls. For longer signals, we find the effects of D_b and c on the archetypal patterns to be qualitatively unchanged (e.g. Figs. S3–S6 show the arrays at $\lambda = 8$ cm). The patterns are weakly sensitive to λ for the reason given earlier. When $\lambda \gg b$, as is typical for signals a few centimetres or longer in ice sheets, the diffusion problem describing isotopic variations at different depths is similar, dominated by horizontal concentration gradients, with terms representing vertical gradients being negligible (footnote 2).

We end the section with a remark useful when considering pattern detection (Sect. 4.1). Since the patterns in Figs. 4 to 9 are based on the normalised H, their δ-variation in absolute terms will be given by their scaled amplitude, as shown by the colour scales or the red and black curves, multiplied by the true amplitude of the vertical bulk signal. For instance, the scaled ampli-tudes of the patterns in Fig. 4b, ≈ 0.12–0.15, translate to δ variations ≈ 0.6–0.75‰ if the bulk signal is 10‰ peak-to-peak. This is both an approximation and an underestimate, because the bulk signal (i.e. section-mean signal in Eq. (15)) always

545   has a scaled amplitude ≲ 1 if short-circuiting operates. We do not calculate the exact conversions here, given an infinite variety
of patterns.

3.2 *Enhancement factor on bulk-ice diffusivity*

Of interest also is how much the presence of grain boundaries affects the enhancement factor f measuring the excess diffusion

550   (and acceleration of signal smoothing) above the rate due to single-crystal diffusion. We study this by examining the computed
surfaces of f as functions of vein-water flow velocity w and signal wavelength λ.

Ng (2023) reported the surfaces $f(w, \lambda)$ at $T = -32$ and -52 °C for the axisymmetric (vein-only) system when $a = 1$ μm

and $b = 1$ mm, which we reproduce in Fig. 12a and 12e as contour maps. Our computed surfaces accounting for grain

boundaries all show the same valley form as these maps, with f increasing with λ and $|w|$. Thus, vein-water flow amplifies

555   excess diffusion in our system (by an amount independent of whether the flow is up or down), as in the vein-only system.

Although not analysed herein, our model also predicts known trends of f against the vein and grain sizes – f increases with a

and decreases with b (Rempel and Wettlaufer, 2003), which reflects the way these parameters control the efficiency and density
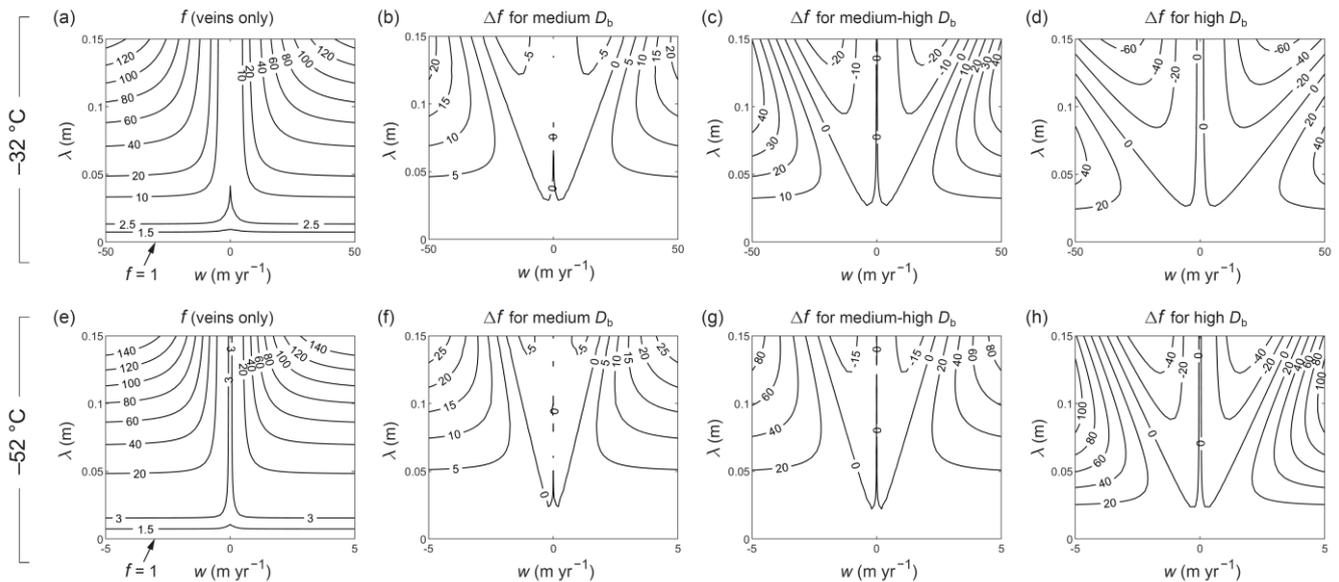
560   Figure 12. Impact of the presence and diffusivity (D_b) of grain boundaries on the level of excess diffusion for different vein-flow velocities
w and signal wavelengths λ at -32°C and -52 °C when $c = 5$ nm. (a, e) Contour maps of enhancement factor $f(w, \lambda)$ for the vein-only system
without grain boundaries; data from Ng (2023). (b–d) $f(w, \lambda)$ reported as contour maps of the difference Δf from (a), for our system at -32
°C when the grain boundaries have medium, medium-high, and high diffusivities. (f–h) Ditto for -52 °C, but referenced to (e).

of short-circuiting elements. Furthermore, our system with grain boundaries exhibits (i) lower f at –52 °C than –32 °C when w
= 0 and (ii) stronger modulation of f by w in colder ice (hence our experiments at –52 °C use lower vein-flow velocities; e.g.
compare the f-values in Fig. 11 resulting from $w = 0.5$ m yr^{-1} to those in Fig. 10 resulting from $w = 5$ m yr^{-1}). These aspects
have been explained by Ng (2023) with scaling arguments that we do not repeat here.

We focus instead on how the surface $f(w, \lambda)$ deforms when we introduce grain boundaries and vary their diffusivity. Fig.
12b–d and f–h present the results at –32 and –52 °C for intermediate grain boundaries with medium, medium-high and high
D_b. The results are shown as difference maps $\Delta f(w, \lambda)$ referenced to the surfaces in Fig. 12a and 12e, because we find
visualising the changes by comparing different sets of contours of f more difficult. (Our computed surfaces at low D_b differ
negligibly from Fig. 12a and 12e and could equally serve as references.) On the difference maps, the interesting feature is the
wedges of negative Δf straddling the $w = 0$ axis. They indicate unexpected reductions in f caused by the grain boundaries when
vein-water flows. The reductions increase in magnitude with D_b and λ, occur at relatively low vein-water velocities in $\lambda \gtrsim 2.5$
cm, and persist to higher vein-water velocities the longer is the signal. Between each pair of wedges is a narrow ridge at $w \approx 0$
where $\Delta f \gtrsim 0$, which matches our finding in Sect. 3.1 that f increases with the degree of grain-boundary short-circuiting at
zero vein flow (e.g. f-values in Figs. 10 and 11). Outside the wedges, Δf increases steeply with λ, $|w|$, and D_b.

For the surfaces $f(\lambda, w)$, these differences mean that grain-boundary short-circuiting flattens their valley bottom (reducing
f there compared to the vein-only case) while it raises f at high vein-flow velocities and for signals shorter than ≈ 2.5 cm – in
the areas outside the wedges. Accordingly, our runs for intermediate grain boundaries and $\lambda = 2$ cm for any w (Sect. 3.1)
predicted more excess diffusion when D_b is increased, whereas for longer signals near a decimetre, raising D_b at $w = 5$ m yr^{-1}
reduced f (see results for $\lambda = 8$ cm in Figs. S3–S6). We have studied the 3D isotopic fields and their phase variations to discern
the mechanism, finding that when vein-water flows, diffusion along grain boundaries suppresses the concentration gradients
(shear layer) induced by the flow by short-circuiting the ice diffusion near the crystal apex. The outcome rests on a competition:
at low $|w|$, this effect overcomes the enhanced isotopic exchange between ice and vein due to the shear layer (so f decreases
overall), but it is out-competed by the latter at high $|w|$ (so f increases). The wedge shape arises because the mechanism is
more effective for long signals, which develop weaker shear layers at a given w. For completeness, we provide the computed
grids of f in the paper's repository and show in Fig. S7 a companion version of Fig. 12 that plots f instead of Δf.

In summary, although short-circuiting by thick or diffusive grain boundaries leaves stable 3-spoke signatures on isotopic
patterns (Sect. 3.1), it does not always increase f. Grain boundaries increase f at zero or high vein-water velocities, but do so
only for short signals at low (non-zero) velocities. Thus, while the presence of grain boundaries or veins in glacier ice ($b \sim$
mm) always causes an excess diffusion compared to the monocrystal, whether grain boundaries amplify its level has a mixed
answer. However, this outcome does not affect the concept of using grain-scale patterns to diagnose isotopic short-circuiting.

4 Discussion

595 4.1 *Detecting isotopic patterns*

Our calculations establish isotopic patterns around triple junctions as an inevitable consequence of excess diffusion that operates by vein and/or grain boundary short-circuiting. This grain-scale prediction should be testable by laboratory measurements on ice samples. As highlighted at the beginning, such tests are needed to verify the Nye–Rempel–Wettlaufer genre of theories. Here we discuss this matter, drawing extensively on the results in Sect. 3.1.

600 The crux is whether such tests reveal systematic excursions in δ around veins and grain-boundaries like the predicted archetypal patterns. Also relevant is whether pole or three-spoke patterns (or both) are found to prevail in natural ice, but current knowledge of grain-boundary properties precludes a clear expectation on this. Our results predict a pattern type dependent on grain-boundary diffusivity and thickness – higher D_b and c favour spokes. Particularly, medium-high to high D_b on our descriptive range (Fig. 2) is needed for spokes (Figs. 10 and 11). This does not necessarily mean that spokes will be rarely 605 observed, given substantial uncertainties about the extent to which impurities and crystallographic factors can affect D_b and c (Sect. 2.2). Also, although the HCl bulk concentration (≈ 0.01 M) used by Lu et al. in their diffusivity measurements to explore the impurity effect is much higher than the typical concentration of Cl$^-$ in ice cores (~ 1–10 μM), natural ice contains myriad impurities. More likely, the detected isotopic patterns might give us a handle to assess the grain-boundary properties.

In terms of measurement technique, one based on laser-ablation (LA) sampling is promising. Bohleber et al. (2021) used 610 LA-ICP-MS (laser ablation inductively-coupled plasma mass spectrometry) to map the elemental abundances (Na, Mg, Sr) on ice-core surface sections at 35 μm resolution, gaining new insights into impurity localisation at grain boundaries; see review by Stoll et al. (2023) also. Importantly, Malegiannaki et al. (2023) have been innovating a system for mapping water isotope ratios in ice by coupling LA sampling with cavity ring down spectroscopy. The resulting isotopic maps will hopefully have a spatial resolution as good as LA-ICP-MS and measurement sensitivity and accuracy on δ^{18}O or δD sufficient for our proposed 615 tests. On our simulated archetypal patterns for $\lambda = 2$ cm, the δ-excursions have widths ~ 10–50% of the grain radius (Figs. 10 and 11) and amplitudes reaching ~ 0.2 of the vertical bulk signal in the more favourable cases (Figs. 4 and 6); that is ~ 1‰ if the bulk-signal variation is 5‰ peak to peak. These values suggest sub-millimetre resolution and sensitivity of a fraction of per mil as broad minimum requirements. However, the predicted pattern amplitudes are weaker in the absence of vein-water flow and much weaker for longer signals (e.g. ~ 0.01–0.05 at $\lambda = 8$ cm). Hence achieving high sensitivity in δ is likely the 620 main obstacle. We think that measurement capabilities of ~ 0.1‰ or better and a few tens of microns are necessary to capture the patterns properly.
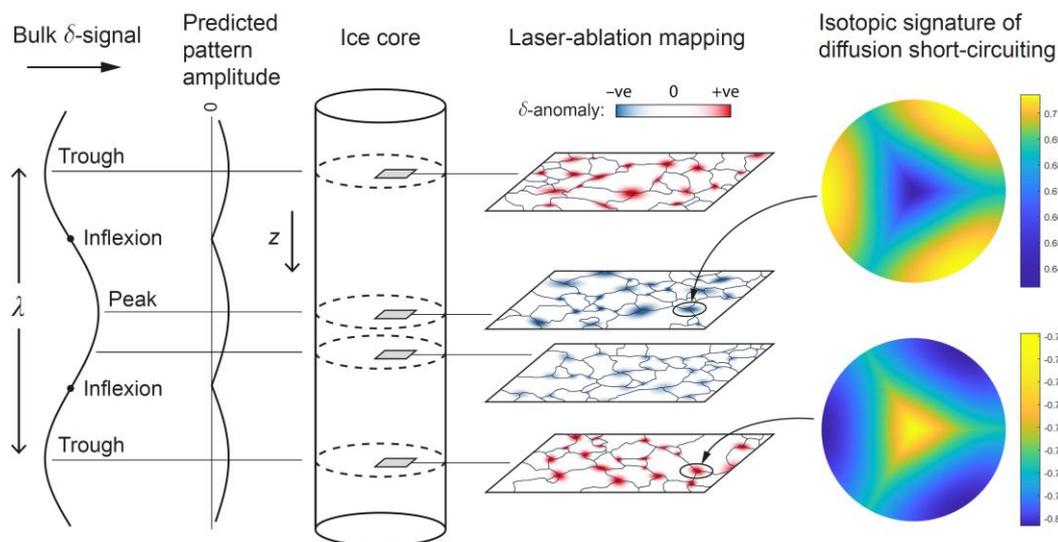
Figure 13. Experimental design for testing ice-core samples for the grain-scale signature of the isotopic short-circuiting causing excess

diffusion. Horizontal sections at the peaks and troughs of the bulk isotopic signal (e.g. δ^{18}O or δD) are expected to show high-amplitude

anomalies in δ around triple junctions if the ice experienced no or negligible vein-water flow ($w \approx 0$). A laser-ablation measurement technique

is used to map these anomalies, some of them resembling the computed patterns in Figs. 4, 5, 6, and 8–11. If $w \approx 0$, sections away from the

peaks and troughs would show weaker anomalies, and sections at the signal inflexion, the faintest anomalies. Cartoons right of centre

illustrate the polarity and amplitude of the mapped patterns; images at far right show how they might look in detail (in the case of spokes).

Our results in Sect. 3.1 show that vein-water flow ($w \neq 0$) would shift the vertical variation of pattern amplitude against the bulk signal.

For testing ice-core samples with this technique, our findings motivate mapping δ on horizontal sections at different

depths. Fig. 13 sketches an experimental design. The bulk isotopic signal should first be determined – e.g. by continuous flow

analysis (CFA) measurements of a vertical strip – to guide where to make horizontal sections. Locations likely to yield stronger

and more detectable isotopic patterns are the peaks and troughs of the bulk signal, away from its inflexions. This is because

when $w = 0$, the transitions where pattern extinction occurs lie at the inflexions, whereas the extrema see the greatest pattern

amplitude (Sect. 3.1; Fig. 4), and because the extrema escape the transitions for all w. This is in turn because vein-water flow

displaces the vein isotopic signals in the direction of w, shifting the transitions back towards (not as far as) the extrema at small

w, and forward again at larger w (Fig. 6; cf. Fig. 4); see also Ng (2023). Given the difficulty of constraining w at ice-core sites

(discussion by Ng) and other factors behind the shift (e.g. uncertain grain-boundary properties in a sample), the amount of shift

is not known a priori, and placing key horizontal sections away from the extrema may risk returning low-amplitude maps.

The map of δ from each horizontal section is processed by subtracting its section-mean value, to isolate variations for

spotting patterns akin to the predicted ones. If 2D mapping is not possible, linear transects may be used to detect anomalies in

δ across grain boundaries. Whether mapping in 1D or 2D, obtaining the grain-boundary network independently by LA-ICP-

645 MS or other measurements is desirable. If multiple sections can be made, we suggest sampling at least at both the bulk-signal peak and trough (Fig. 13) to look for the predicted pattern sign reversal, associated with those stretches where isotopes diffuse towards and away from veins in the short-circuiting (Sect. 3.1). Additional sections can sample at quarter-wave locations (Fig. 13) or nearer the inflexions to characterise how pattern amplitudes vary with depth relative to the bulk signal. For ice affected by short-circuiting, our model predicts (i) same-signed patterns on each horizontal section (triple junctions all showing either

650 higher or lower δ than away from them) and (ii) pattern amplitudes cycling vertically on half the bulk-signal wavelength (phase shift between this cycle and the bulk signal would indicate vein-water flow). Indeed, firm evidence for isotopic short-circuiting includes finding these depth-dependent relationships, besides the archetypal patterns.

On maps of δ yielding successful detection, we expect to see more varieties of triple-junction patterns than simple poles and spokes – patterns with different shape, amplitudes (perhaps even some with opposite sign), levels of distortion, and patterns

655 unlike the archetypes. Reasons include (i) a non-sinusoidal bulk signal, (ii) anisotopy in the diffusivity D_s within crystals, (iii) curved grain boundaries and triple-junction angles deviating from 120° in real ice, (iv) textural variations in real ice (i.e. different vein diameters, grain sizes and shapes, and triple-junction axial orientations (Fig. 9) sampled by the horizontal section – recall that our simulations used fixed a and b), and (v) "out of plane" effects of veins and grain boundaries slightly above and below the section (discussed later in Sect. 4.2). Based on the computed pattern arrays in Figs. 10 and 11, an observed

660 assemblage of archetypal or near-archetypal patterns may allow us to gauge the short-circuiting regime: spoke- (/pole-) dominated assemblages would suggest thick, diffusive (/thin, non-diffusive) grain-boundaries.

Vertical sections can also be mapped in the experiments. They will miss most (if not all) vertically-oriented triple junctions and hence not show our predicted patterns, but the out-of-plane effects may generate excursions near triple junctions (Sect. 4.2). Taking random linear transects across the charted patterns in Sect. 3.1 (e.g. Figs. 4 to 6) suggests that δ-excursions

665 should occur around some grain boundaries in affected ice samples. Again, our model predicts their amplitude to vary vertically in unison – not necessarily in phase – with the bulk signal.

For isotopic maps from either vertical sections or a stack of horizontal sections, consistent phase relationship found between the pattern amplitudes and the bulk signal can be used to infer the direction and relative magnitude of vein-water flow (or its stagnancy). For ice-core samples, this means the w experienced when they were in-situ in the ice column.

670 Which ice-core samples should be tested? High on the list are those from the Holocene part of the GRIP core (Johnsen et al., 1997, 2000), $\approx$ 15–18 ka BP in the WAIS Divide core (Jones et al. 2017), and MIS 19 ($\sim$ 3170 m) in the EPICA Dome C (Pol et al., 2010) – given interpretation that they suffered excess diffusion (Sect. 1). Specifically, our model suggests choosing samples carrying bulk signals that are short ($\lambda \sim$ a few cm, if possible) with high amplitude, as these promote strong patterns. But since diffusion (especially excess diffusion) damps short signals efficiently, ideal samples may be difficult to

675   find, and we anticipate severe demands on the measurement sensitivity and the need to compromise between amplitude and wavelength. Separately, although the ice-column temperature of the samples and the time span of the bulk signal (e.g. whether it is annual, centennial, or millennial) do not matter in these tests for excess diffusion, samples with high dust or microparticle content are best avoided because blockage of veins (maybe grain boundaries also) hinders the theorised short-circuiting. We pause with these general ideas on sample selection here and leave dedicated considerations to future studies.

680   It is equally important to test ice-core samples apparently unaffected by excess diffusion. Together with the (purportedly) affected samples, they may help us understand the origin and pattern of occurrence of excess diffusion in individual or different cores. From the perspective of the Nye–Rempel–Wettlaufer framework, which includes Ng's (2023) and our present model, it is in fact puzzling why excess diffusion occurs in a patchy manner – not everywhere – in ice cores. All three cores mentioned above have other sections where the signal decay rate (or diffusion lengths) can be explained with monocrystalline diffusivity

685   – without invoking excess diffusion. Yet the theories predict $f > 1$ always, because veins and grain boundaries are always present. One possibility is that blocked or disconnected veins prevent excess diffusion on some stretches, whereas on other stretches, dissolved impurities migrate to grain boundaries (e.g. Bohleber et al., 2021) and then to the veins, thickening them to switch on excess diffusion. A study that tests both unaffected and affected samples for grain-scale isotopic short-circuiting and maps their impurity distribution simultaneously (e.g. with LA-ICP-MS) might shed light on the enigma.

690   Artificial ice samples can be tested also. Fabricating these with bulk isotopic signals may be non-trivial, and the long time for isotopic patterns to stabilise seems impractical (the time scale b^2/D_s in Eq. (17) gives 16, 27, and 78 years at –5, –10, and –20 °C, respectively, for $b = 1$ mm) and may limit the insights to the transient stages of short-circuiting.

4.2 *Model limitations and extensions*

695   Real isotopic patterns at the grain scale will be more varied and complex than predicted here because our model geometry is highly idealised: its cell-like regularity (Fig. 1) ignores grain size and shape variations, for instance (Sect. 4.1). Before finishing, we consider two important limitations of the model in this respect and how they may affect our findings.

        First, the true geometry has many non-vertical veins and grain boundaries. To gauge their effects in a more realistic model, one might try to add horizontal veins and grain boundaries to the model geometry. Ice with grain size $b \sim$ mm will have

700   many such elements in one λ (if $\lambda \sim$ cm to dm). Spaced at intervals $\sim b$, they extend the diffusion pathways laterally from our system. We expect the associated δ-excursions, which modify the isotopic field near these elements, to be thin vertically, just as the radial (/azimuthual) excursions around veins (/grain boundaries) in our current model are thin. Between these new excursions, the field should resemble the one computed by us. Therefore, on horizontal maps of δ, we should still find triple-junction patterns like the predicted ones, for neighbouring grains crossed by the section near their waist (thick excursions from

705   high c and D_b might distort these patterns). But grains crossed near their top and bottom will show strongly-affected patterns, as their sampled junctions and boundaries lie near or within the new excursions. Consequently, real maps of δ will exhibit

various out-of-plane distortion due to horizontal and sub-horizontal veins and grain boundaries above and below the section. The impact of the (sub-)horizontal elements on excess diffusion is harder to predict. They might increase the isotopic exchange between the veins and ice to raise f overall, or short-circuit the vertical system sufficiently to reduce f (we gather this possibility

710 from Sect. 3.2, where we saw how grain boundaries weaken the flow-induced shear layer around veins).

Second, veins and grain boundaries in the real system generally are not stationary as assumed but migrate continually. Their 3D motion must cause lopsided or asymmetric isotopic patterns. Modelling the outcome will require quantifying the relative rates of isotopic-field evolution and this motion, accounting for the statistical distribution of vein and grain-boundary velocities and impurity factors, which lies beyond the scope of this paper.

715 These limitations apply also to the theories of excess diffusion by Nye (1998), Johnsen et al. (2000), Rempel and Wettlaufer (2003), and Ng (2023). Studies using the enhancement factor f modelled by us or those studies to simulate signal evolution and diffusion-length profiles in ice cores should bear them in mind.

In terms of building more realism and sophistication upon Nye's original model, we are near the end of the road with using simple analytical models to capture the coupled diffusion across ice, veins, and grain boundaries. Looking forward,

720 overcoming the geometrical limitations seems challenging and may require approximate approaches (e.g. using multiscale or homogenisation methods to derive bulk diffusivity) or direct numerical simulation dealing with complex mobile interfaces.

5 Conclusions

If short-circuiting by diffusion in veins and grain boundaries is responsible for excess diffusion in ice, then isotopic imprints similar to our computed archetypal pole and spoke patterns will occur at the grain scale. The δ-excursion of each imprint

725 reflects isotopic exchange between ice and the short-circuiting pathways, its polarity showing whether the pathways act as a sink or source of isotopes for the adjacent crystal lattice. For ice with grain radius $b = 1$ mm, our model predicts excursions $\sim$ $0.1b - 0.5b$ wide ($\sim 10^{-1}$ mm), with δ-variations proportional to the amplitude of the bulk isotopic signal and ranging up to a fraction of ~ 0.2 of that signal, but typically smaller. Mapping the isotopic patterns in detail probably requires a minimum instrumental sensitivity of ~ 0.1‰ and a spatial resolution of a few tens of microns or better. Pattern detectability is improved

730 in ice that experienced vein-water flow in the ice column, because this amplifies the excursions.

These predictions motivate testing ice samples for these signatures of excess diffusion and the short-circuiting mechanism by mapping their isotopic concentration at high resolution. Given ongoing development of laser-ablation measurement techniques by some workers, we outlined a laboratory scheme for conducting the tests on 2D sections of ice from ice cores, together with thoughts on sample selection (Sect. 4.1; Fig. 13). The proposed tests are independent from known ways of

735 inferring excess diffusion from the signal-decay rates or estimated diffusion lengths on ice-core isotope profiles, which can diagnose its occurrence, but not the underlying mechanism.

Our modelling elucidates the controls on the isotopic signatures. Although the isotopic diffusivity (D_b) and thickness (c) of grain boundaries in ice are poorly constrained and may be highly variable, our results show that thin, non-diffusive grain boundaries yield pole patterns, whereas thick, diffusive grain boundaries (including those due to high impurity levels) yield spoke patterns. Figs. 10 and 11 show the predicted continuum of pattern types on the c–D_b parameter space, which can be used with the observed isotopic patterns in an ice sample to infer its grain-boundary properties in relative terms. The grain-boundary diffusivity affects the pattern via the parameter $\beta_b = D_b/D_s - 1$, in which D_b and the monocrystalline diffusivity D_s both depend on temperature (Fig. 2). Our results also revise current estimates of the enhancement factor f that quantifies the excess diffusion above D_s. For the full system with veins and grain boundaries, vein-water flow is found to amplify excess diffusion and increase f, as in the vein-only system (Ng, 2023). However, at a fixed (non-zero) vein-water flow velocity w, the presence of grain boundaries can increase or reduce f compared to the vein-only system, depending on the signal wavelength; at sufficiently high w, f is increased for decimetre-scale or shorter signals (Sect. 4.2). The model predicts polycrystalline ice always to exhibit some excess diffusion ($f > 1$) unless the vein network is blocked by solid particles or disconnected.

In future extensions, it may be possible to find ways of using the assemblage of grain-scale isotopic patterns in ice samples to quantify their level of excess diffusion, and thus constrain vein and grain-boundary properties. The proposed laboratory test and this avenue will help us understand why excess diffusion occurs on some sections of ice cores and not others.

Code and data availability

The MATLAB code for solving the model equations and computed grids of the enhancement factor are archived at https://doi.org/10.15131/shef.data.xxxxxxxx. Use https://figshare.com/s/e42a421e53b02efdaa0f during the review stage.

Video supplement

Movies S1–S7 are available at https://doi.org/10.15131/shef.data.xxxxxxxx.
Please use https://figshare.com/s/37cfa936be37610f24e8 during the review stage.

Supplement

Section S1, Movies S1–S7, and Figures S1–S7 are available at https://doi.org/10.15131/shef.data.xxxxxxxx.
Please use https://figshare.com/s/37cfa936be37610f24e8 during the review stage.

Author contribution

F. S. L. Ng designed the study, performed all analyses, and wrote the paper.

Competing interests

The author has declared that there are no competing interests.

Acknowledgements

I thank the City University of Hong Kong for library access during my visits, which gave me a peaceful environment for doing some of the calculations in this study.

References

Benatov, L. and Wettlaufer, J. S.: Abrupt grain boundary melting in ice, Phys. Rev. E, 70, 061606, https://doi.org/10.1103/PhysRevE.70.061606, 2004.

Boyd, J. P.: Chebyshev and Fourier Spectral Methods (Second Edition), Dover Publications, ISBN-13 978-0486411835, 2000.

Bohleber, P., Roman, M., Šala, M., Delmonte, B., Stenni, B., and Barbante, C.: Two-dimensional impurity imaging in deep Antarctic ice cores: snapshots of three climatic periods and implications for high-resolution signal interpretation, The Cryosphere, 15, 3523–3538, https://doi.org/10.5194/tc-15-3523-2021, 2021.

Brox, T. I., Skidmore, M. L., and Brown, J. R.: Characterizing the internal structure of laboratory ice samples with nuclear magnetic resonance, J. Glaciol., 61, 55–64, https://doi.org/10.3189/2015JoG14J133, 2015.

Dash, J. G., Rempel, A. W., and Wettlaufer, J. S.: The physics of premelted ice and its geophysical consequences, Revs. Mod. Phys., 78, 695–741, https://doi.org/10.1103/RevModPhys.78.695, 2006.

Gillen, K. T., Douglass, D. C., and Hoch, M. J. R.: Self-diffusion in liquid water to –31°C, J. Chem. Phys., 57(12), 5117–5119, 1972.

Grisart, A., Casado, M., Gkinis, V., Vinther, B., Naveau, P., Vrac, M., Laepple, T., Minster, B., Prié, F., Stenni, B., Fourré, E., Steen-Larsen, H. C., Jouzel, J., Werner, M., Pol, K., Masson-Delmotte, V., Hoerhold, M., Popp, T., and Landais, A.: Sub-millennial climate variability from high-resolution water isotopes in the EPICA Dome C ice core, Clim. Past, 18, 2289–2301, https://doi.org/10.5194/cp-18-2289-2022, 2022.

Johnsen, S. J.: Stable isotope homogenization of polar firn and ice. International Association of Hydrological Sciences Publication 118 (Symposium at Grenoble 1975: Isotopes and Impurities in Snow and Ice), 210–219, 1977.

Johnsen, S. J., Clausen, H. B., Dansgaard, W., Gundestrup, N. S., Hammer, C. U., Andersen, U., Andersen, K. K., Hvidberg, C. S., Dahl-Jensen, D., Steffensen, J. P., Shoji, H.,Sveinbjörnsdóttir, Á. E., White, J., Jouzel, J., and Fisher, D.: The δ^{18}O record along the Greenland Ice Core Project deep ice core and the problem of possible Eemian climatic instability, J. Geophys. Res. Oceans, 102(C12), 26397–26410, https://doi.org/10.1029/97JC00167, 1997.

Johnsen, S. J., Clausen, H. B., Cuffey, K. M., Hoffmann, G., Schwander, J., and Creyts, T.: Diffusion of stable isotopes in polar firn and ice: the isotope effect in firn diffusion. In Hondoh, T., ed. Physics of ice core records. Sapporo, Hokkaido University Press, 121–140, 2000.

Jones, T. R., Cuffey, K. M., White, J. W. C., Steig, E. J., Buizert, C., Markle, B. R., McConnell, J. R., and Sigl, M.: Water isotope diffusion in the WAIS Divide ice core during the Holocene and last glacial, J. Geophys. Res. Earth Surf., 122, 290–309, https://doi.org/10.1002/2016JF003938, 2017.

Lu, H., McCartney, S. A., and Sadtchenko, V.: Fast thermal desorption spectroscopy study of H/D isotopic exchange reaction in polycrystalline ice near its melting point, J. Chem. Phys. 127, 184701, https://doi.org/10.1063/1.2786101, 2007.

Lu, H., McCartney, S. A., and Sadtchenko, V.: H/D exchange kinetics in pure and HCl doped polycrystalline ice at temperatures near its melting point: Structure, chemical transport, and phase transitions at grain boundaries, J. Chem. Phys. 130, 054501. https://doi.org/10.1063/1.3039077, 2009.

Lundy, T. S.: Use of the Hart–Mortlock equation to interpret tracer diffusion results, Scripta Metallurgica, 12, 95–98, 1978.

Mader, H. M.: Observations of the water-vein system in polycrystalline ice, J. Glaciol., 38, 333–347, 1992a.

Mader, H. M.: The thermal behaviour of the water-vein system in polycrystalline ice, J. Glaciol., 38, 359–374, 1992b.

Malegiannaki, E., Peensoo, K. M., Bohleber, P., and Gkinis, V.: Challenges of water-isotope measurements on ice cores, PAGES Magazine, 31(2), 64-65, doi.org/10.22498/pages.31.2.64, 2023.

Moreira, P. A. F. P., Veiga, R. G. D., De Almeida Ribeiro, I., Freitas, R., Helfferichf, J., and De Koning, M.: Anomalous diffusion of water molecules at grain boundaries in ice Ih, Phys. Chem. Chem. Phys., 20, 13944, https://doi.org/10.1039/c8cp00933c, 2018.

Mulvaney, R., Wolff, E. W., and Oates, K.: Sulphuric acid at grain boundaries in Antarctic ice, Nature, 331, 247–249, 1988.

Ng, F. S. L.: Pervasive diffusion of climate signals recorded in ice-vein ionic impurities, The Cryosphere, 15, 1787–1810, https://doi.org/10.5194/tc-15-1787-2021, 2021.

Ng, F. S. L.: Isotopic diffusion in ice enhanced by vein-water flow, The Cryosphere, 17, 3063–3082, https://doi.org/10.5194/tc-17-3063-2023, 2023.

Ng, F.: Numerical code of the study "The grain-scale signature of isotopic diffusion in ice", Figshare [code and data set], https://doi.org/10.15131/shef.data.xxxxxxxx, 2024a. (Please use https://figshare.com/s/e42a421e53b02efdaa0f during the review stage.)

Ng, F.: Supplement of the study "The grain-scale signature of isotopic diffusion in ice", University of Sheffield [text, video, and figures], https://doi.org/10.15131/shef.data.xxxxxxxx, 2024b. (Use https://figshare.com/s/37cfa936be37610f24e8 during the review stage.)

Nye, J. F.: The geometry of water veins and nodes in polycrystalline ice, J. Glaciol., 35, 17–22, 1989.

Nye, J. F.: Thermal behaviour of glacier and laboratory ice, J. Glaciol., 37(127), 401–13, 1991.

Nye, J. F.: Diffusion of isotopes in the annual layers of ice sheets, J. Glaciol., 44(148), 467–468, 1998.

Pol, K., Masson-Delmotte, V., Johnsen, S., Bigler, M., Cattani, O., Durand, G., Falourd, S., Jouzel, J., Minster, B., Parrenin, F., Ritz, C., Steen-Larsen, H. C., and Stenni, B.: New MIS 19 EPICA Dome C high resolution deuterium data: Hints for a problematic preservation of climate variability at sub-millennial scale in the "oldest ice", Earth Planet. Sc. Lett., 298, 95–103, https://doi.org/10.1016/j.epsl.2010.07.030, 2010.

Prielmeier, F. X., Lang, E.W., Speedy, R. J., and Lüdemann, H.-D.: The pressure dependence of self diffusion in supercooled light and heavy water, Ber. Bunsenges. Phys. Chem., 92, 1111–1117, 1988.

Ramseier, R. O.: Self-diffusion of tritium in natural and synthetic ice monocrystals, J. Appl. Phys., 38(6), 2553–2556, 1967.

Rempel, A.: Englacial phase changes and intergranular flow above subglacial lakes, Ann. Glaciol., 40, 191-194, 2005.

Rempel, A. W. and Wettlaufer, J. S.: Isotopic diffusion in polycrystalline ice, J. Glaciol., 49(166), 397–406, 2003.

Stoll, N., Bohleber, P., Dallmayr, R., Wilhelms, F., Barbante, C., and Weikusat, I.: The new frontier of microstructural impurity research in polar ice, Ann. Glaciol., First View, 1–4, https://doi.org/10.1017/aog.2023.61, 2023.

Thomson, E. S., Hansen-Goos, H., Wettlaufer, J. S., Wilen, L. A.: Grain boundary melting in ice, J. Chem. Phys., 138, 124707, https://doi.org/10.1063/1.4797468, 2013.

Trefethen, L. N.: Spectral methods in MATLAB, Society for Industrial and Applied Mathematics (SIAM), ISBN 0-89871-465-6, 2000.

Wettlaufer, J. S.: Impurity effects in the premelting of ice, Phys. Rev. Letts., 82, 2516–2519, 1999.

Whillans, I. M. and Grootes, P. M: Isotopic diffusion in cold snow and firn, J. Geophys. Res., 90(D2), 3910–3918, https://doi.org/10.1029/JD090iD02p03910, 1985.

Xu, Y., Petrika, N. G., Smith, R. S., Kay, B. D., and Kimmel, G. A.: Growth rate of crystalline ice and the diffusivity of supercooled water from 126 to 262 K, PNAS, 113(52), 14921–14925, https://doi.org/10.1073/pnas.1611395114, 2016.

Yagasaki, T., Matsumoto, M., and Tanaka, H.: Molecular dynamics study of grain boundaries and triple junctions in ice, J. Chem. Phys., 153, 124502, https://doi.org/10.1063/5.0021635, 2020.